





Formation of GW190521 from stellar evolution: the impact of the hydrogen-rich envelope, dredge-up, and $^{12}\text{C}(\alpha, \gamma)^{16}\text{O}$ rate on the pair-instability black hole mass gap

Guglielmo Costa ^{1,2,3}★ Alessandro Bressan,^{3,4} Michela Mapelli ^{1,2,3} Paola Marigo,¹ Giuliano Iorio ^{1,2,3} and Mario Spera ⁴

¹Dipartimento di Fisica e Astronomia Galileo Galilei, Università di Padova, Vicolo dell'Osservatorio 3, I-35122 Padova, Italy

²INFN-Padova, Via Marzolo 8, I-35131 Padova, Italy

³INAF-Padova, Vicolo dell'Osservatorio 5, I-35122 Padova, Italy

⁴SISSA, via Bonomea 365, I-34136 Trieste, Italy

Accepted 2020 December 15. Received 2020 December 15; in original form 2020 October 1

ABSTRACT

Pair-instability (PI) is expected to open a gap in the mass spectrum of black holes (BHs) between ≈ 40 – 65 and ≈ 120 M_{\odot} . The existence of the mass gap is currently being challenged by the detection of GW190521, with a primary component mass of 85^{+21}_{-14} M_{\odot} . Here, we investigate the main uncertainties on the PI mass gap: the $^{12}\text{C}(\alpha, \gamma)^{16}\text{O}$ reaction rate and the H-rich envelope collapse. With the standard $^{12}\text{C}(\alpha, \gamma)^{16}\text{O}$ rate, the lower edge of the mass gap can be 70 M_{\odot} if we allow for the collapse of the residual H-rich envelope at metallicity $Z \leq 0.0003$. Adopting the uncertainties given by the STARLIB database, for models computed with the $^{12}\text{C}(\alpha, \gamma)^{16}\text{O}$ rate -1σ , we find that the PI mass gap ranges between ≈ 80 and ≈ 150 M_{\odot} . Stars with $M_{\text{ZAMS}} > 110$ M_{\odot} may experience a deep dredge-up episode during the core helium-burning phase, that extracts matter from the core enriching the envelope. As a consequence of the He-core mass reduction, a star with $M_{\text{ZAMS}} = 160$ M_{\odot} may avoid the PI and produce a BH of 150 M_{\odot} . In the -2σ case, the PI mass gap ranges from 92 to 110 M_{\odot} . Finally, in models computed with $^{12}\text{C}(\alpha, \gamma)^{16}\text{O} -3\sigma$, the mass gap is completely removed by the dredge-up effect. The onset of this dredge-up is particularly sensitive to the assumed model for convection and mixing. The combined effect of H-rich envelope collapse and low $^{12}\text{C}(\alpha, \gamma)^{16}\text{O}$ rate can lead to the formation of BHs with masses consistent with the primary component of GW190521.

Key words: convection – stars: black holes – stars: evolution – stars: interiors – stars: massive – stars: mass-loss.

1 INTRODUCTION

The LIGO-Virgo collaboration (LVC) recently reported the discovery of GW190521 (Abbott et al. 2020b,e). With a primary black hole (BH) mass of 85^{+21}_{-14} M_{\odot} and a secondary BH mass of 66^{+17}_{-18} M_{\odot} (90 per cent credible intervals), this binary black hole (BBH) merger is the most massive one observed with gravitational waves to date (Abbott et al. 2016a,b,c, 2019a,b, 2017, 2020a,c,d). The mass of the primary BH is a puzzle for astrophysicists, because it lies in the middle of the pair-instability (PI) mass gap.

PI is possibly the key process to understand the maximum mass of stellar-origin BHs, because it is expected to carve a gap in the mass spectrum of BHs between ≈ 40 – 65 and ≈ 120 M_{\odot} (e.g. Heger & Woosley 2002; Woosley, Blinnikov & Heger 2007; Belczynski et al. 2016; Spera & Mapelli 2017; Woosley 2017, 2019; Giacobbo, Mapelli & Spera 2018; Mapelli et al. 2019; Spera et al. 2019; Tanikawa et al. 2020a). The uncertainty on the boundaries of the PI mass gap depends on a number of physical processes (e.g. Takahashi 2018; Leung, Nomoto & Blinnikov 2019; Marchant et al. 2019; Stevenson et al. 2019; Farmer et al. 2019, 2020; Mapelli et al. 2020; Renzo et al. 2020; Tanikawa et al. 2020b; van Son et al. 2020).

PI starts to be efficient when the plasma inside stars reaches temperatures above 6×10^8 K and densities between about 10^2 and 10^6 g cm^{-3} . Such conditions on internal temperature and density are reached when massive CO cores are formed in stars. Pair creation converts thermal energy into rest mass of $e^- e^+$, lowering the central pressure. This causes an hydro-dynamical instability that leads to core collapse. In the collapsing core, oxygen is ignited explosively.

In stars developing a helium core mass ≈ 32 – 64 M_{\odot} at the end of carbon burning, PI manifests as pulsational PI (PPI): the star starts to pulsate losing a large amount of mass, until it finds a new equilibrium. After PPI, the star will end its life with a core-collapse supernova or a direct collapse, leaving a BH. More massive stars, with helium core mass ≈ 64 – 135 M_{\odot} , undergo a pair-instability supernova (PISN): a powerful single pulse that totally destroys the star, leaving no compact remnant. Finally, PI triggers the direct collapse of stars with He core mass > 135 M_{\odot} , eventually producing an intermediate-mass BH (Heger & Woosley 2002). Such theoretical picture has been confirmed by many authors in both 1D (Heger & Woosley 2002; Woosley 2017; Takahashi 2018; Marchant et al. 2019) and multi-dimensional hydrodynamical simulations (Chatzopoulos, Wheeler & Couch 2013; Chen et al. 2014). From an observational perspective, iPTF14hls (Arcavi et al. 2017) and SN 2016iet (Gomez et al. 2019) cannot be explained by current core-collapse supernova models and might be connected with PI.

* E-mail: guglielmo.costa@unipd.it

If a massive star enters or not in the PI regime depends mainly on the CO core mass left after the central He burning and on its evolution during the following advanced phases. For a given zero-age main sequence (ZAMS) mass (M_{ZAMS}) and stellar metallicity (Z), the final CO mass can be strongly affected by many evolutionary processes, such as mass-loss, convection, overshooting, semi-convection (Kaiser et al. 2020; Clarkson & Herwig 2020; Renzo et al. 2020), rotation (Chatzopoulos & Wheeler 2012; Limongi & Chieffi 2018; Song et al. 2020; Marchant & Moriya 2020; Mapelli et al. 2020) and internal and surface magnetic fields (Haemmerlé & Meynet 2019; Keszthelyi et al. 2020). These processes may change the ZAMS mass versus CO core mass relation and, thus, the initial mass at which stars enter in the PI regime (Takahashi 2018). Another important ingredient that influences both the CO core mass and its composition is represented by nuclear reactions during the core helium burning (CHeB). The two most important ones are the triple- α reaction, ${}^4\text{He}(2\alpha, \gamma){}^{12}\text{C}$, and the carbon- α one, ${}^{12}\text{C}(\alpha, \gamma){}^{16}\text{O}$. The interplay of these two reactions during the CHeB phase determines the final carbon-to-oxygen ratio (${}^{12}\text{C}/{}^{16}\text{O}$) in the CO core, hence the final fate of the star (Weaver & Woosley 1993). The ${}^{12}\text{C}(\alpha, \gamma){}^{16}\text{O}$ reaction rate is one of the most uncertain (Caughlan & Fowler 1988; Buchmann 1996; Sallaska et al. 2013; deBoer et al. 2017; Rapagnani et al. 2017), because it is difficult to measure. The study on how the ${}^{12}\text{C}(\alpha, \gamma){}^{16}\text{O}$ reaction affects the stellar evolution is an old problem (Iben 1967; Brunish & Becker 1990; Alongi et al. 1991). In recent years, many efforts have been done to understand its importance on the most advanced stellar phases and in the final fates (Woosley & Heger 2007; Tur, Heger & Austin 2007, 2010; deBoer et al. 2017; Fields et al. 2018; Takahashi 2018; Farmer et al. 2019; Sukhbold & Adams 2020; Farmer et al. 2020).

In particular, Farmer et al. (2019) and Farmer et al. (2020) show that the ${}^{12}\text{C}(\alpha, \gamma){}^{16}\text{O}$ reaction rate is one of the main sources of uncertainty on the boundaries of the PI mass gap, when pure helium stars are considered. Another major source of uncertainty on the final BH mass is the fate of the residual hydrogen envelope in case of a direct collapse: if a massive star retains a fraction of its H envelope to the very end of its life, is this envelope able to collapse together with the internal layers of the star? Or is it so loosely bound that it is expelled, even without a supernova explosion (Sukhbold et al. 2016)? If the residual H envelope collapses to the final BH, the lower edge of the PI mass gap (M_{gap}) might increase by $\approx 20 M_{\odot}$ (Mapelli et al. 2020).

The main focus of this work is to study the effect of the uncertainty of the ${}^{12}\text{C}(\alpha, \gamma){}^{16}\text{O}$ reaction rate on the M_{gap} in metal-poor stars. With respect to Farmer et al. (2020), who consider only pure-helium stars, we also investigate stars with hydrogen envelopes. This enables us to model the PI mass gap accounting for the possible collapse of the residual H envelope. Moreover, we find that the onset of a dredge-up during the H shell burning phase plays a crucial role for the evolution of the CO core of the most massive stars. The PI mass gap might even disappear for the combined effect of envelope undershooting and low ${}^{12}\text{C}(\alpha, \gamma){}^{16}\text{O}$ reaction rate. Our goal is to determine under which conditions the formation of BHs like the primary component of GW190521 (Abbott et al. 2020b,e) is possible through single stellar evolution.

In Section 2, we give a description of the PARSEC code, we describe the method adopted to include different ${}^{12}\text{C}(\alpha, \gamma){}^{16}\text{O}$ reaction rates and how we test the stellar dynamical stability during the evolution. In Section 3, we present the new PARSEC evolutionary tracks of pure-He stars computed with varying ${}^{12}\text{C}(\alpha, \gamma){}^{16}\text{O}$ reaction rates and compare them with the results by other authors. In Section 4, we present the new tracks of massive stars with hydrogen envelopes and

compare the maximum masses found for the M_{gap} with other studies. Finally, in section 6 we draw our conclusions.

2 METHODS

In this work, we use the PARSEC V2.0 code that has been extensively described in Costa et al. (2019) and references therein. In the following, we describe the major updates adopted for this work.

2.1 Winds of massive stars

Mass-loss by stellar winds is modelled as described in Chen et al. (2015). For massive hot stars, we take into account the dependence of mass loss on both stellar metallicity (Vink, de Koter & Lamers 2000, 2001) and Eddington ratio (Gräfener & Hamann 2008; Vink 2011). With this mass loss, the models are able to reproduce the Humphreys-Davidson limit (Humphreys & Davidson 1984) observed in the Galactic and Large Magellanic Cloud (LMC) colour-magnitude diagrams¹ (Chen et al. 2015). The metallicity dependence of mass loss is expressed as a dependence on the surface iron abundance.²

For Wolf-Rayet (WR) stars, we adopt the new revised mass-loss prescription by Sander et al. (2019):

$$\text{Log} \frac{\dot{M}}{M_{\odot} \text{ yr}^{-1}} = -8.31 + 0.68 \text{Log} \frac{L}{L_{\odot}}. \quad (1)$$

This relation is a good fit for Galactic WR type-C (WC) and WR type-O (WO) stars (as shown in fig. 5 of Sander et al. 2019) but, as such, it does not include a metallicity dependence which is of paramount importance for our work. In order to include a metallicity dependence in equation (1), we use the results by Vink (2015). From models of WN and WC stars at varying Fe and C–O abundances, Vink (2015) concludes that the main driver of mass-loss is Fe and that the eventual surface C excess in WC stars only produces a lower limit threshold for the mass-loss rate. By fitting Vink (2015) models of WN and WC stars at varying surface Fe abundance, we derive two multiplicative factors (for WN and WC stars, respectively) to be applied to equation (1):

$$f_{\text{WN}} = -1 + 1.9 \tanh \{0.58 [\text{Log}(X_{\text{Fe}}) + 1]\}, \quad (2)$$

$$f_{\text{WCO}} = -0.3 + 1.2 \tanh \{0.5 [\text{Log}(X_{\text{Fe}}) + 0.5]\} \quad (3)$$

where X_{Fe} is the mass fraction iron content.

These two factors are obtained by fitting models of WN and WC/WO stars in which mass-loss mainly depends on iron and, to a lesser extent, on CNO elements (Vink 2015). When metallicity decreases, the mass-loss rate lowers and flattens to values given by the CNO elements (see fig. 2 in Vink 2015). It is unlikely that the WR mass-loss depends on the helium surface content which, instead, is likely the result of a high mass-loss rate (Bestenlehner et al. 2014).

2.2 Opacity, neutrinos, and equation of state

In the high-temperature regime, $4.2 \leq \log(T/\text{K}) \leq 8.7$, we adopt the opacity tables provided by the Opacity Project At Livermore

¹We do not have calibrations at lower metallicity than the LMC one, thus, an uncertainty on the mass loss remains. A recent study by Jiang et al. (2018) on mass outburst on luminous blue variable stars using detailed 3D simulations found outburst episodes that lead to instantaneous mass-loss rate of $\approx 0.05 M_{\odot} \text{ yr}^{-1}$, at solar metallicity.

²Thus, when using the fitting formulas from Vink (2011), the iron content must be re-scaled to the iron content assumed for the Sun in Vink et al. (2001).

Table 1. List of the nuclear reaction rates added to PARSEC v2.0 in this work.

Reaction	Reference
$^{16}\text{O}(\alpha, \gamma)^{20}\text{Si}$	Caughlan & Fowler (1988)
$^{28}\text{Si}(\alpha, \gamma)^{32}\text{S}$	Cyburt et al. (2010)
$^{32}\text{S}(\alpha, \gamma)^{36}\text{Ar}$	Cyburt et al. (2010)
$^{36}\text{Ar}(\alpha, \gamma)^{40}\text{Ca}$	Cyburt et al. (2010)
$^{40}\text{Ca}(\alpha, \gamma)^{44}\text{Ti}$	Cyburt, Hoffman & Woosley (2012)
$^{44}\text{Ti}(\alpha, \gamma)^{48}\text{Cr}$	Cyburt et al. (2010)
$^{48}\text{Cr}(\alpha, \gamma)^{52}\text{Fe}$	Cyburt et al. (2010)
$^{52}\text{Fe}(\alpha, \gamma)^{56}\text{Ni}$	Cyburt et al. (2010)
$^{56}\text{Ni}(\alpha, \gamma)^{60}\text{Zn}$	Cyburt et al. (2010)

Note. This table reports only the reactions that were added to PARSEC in this work. The other reactions, already included in the previous versions of the code, can be found in Table 1 of Fu et al. (2018).

(OPAL)³ team (Iglesias & Rogers 1996, and references therein), in the low-temperature regime, $3.2 \leq \log(T/\text{K}) \leq 4.1$, we employ the \mathcal{A} SOPUS tool⁴ (Marigo & Aringer 2009). Conductive opacities are included following Itoh et al. (2008).

Energy losses by electron neutrinos are taken from Munakata, Kohyama & Itoh (1985) and Itoh & Kohyama (1983), and for plasma neutrinos we use the fitting formulae by Haft, Raffelt & Weiss (1994).

To compute the equation of state (EOS) of stellar matter, we adopt two different models, depending on central temperature. For temperature $\log(T/\text{K}) < 8.5$, we adopt the FREEEOS⁵ code version 2.2.1 by Alan W. Irwin. As already described in Bressan et al. (2012), this code is integrated within our evolutionary code so we can obtain the EOS in two ways: we can compute it on-the-fly, with a higher degree of accuracy, but with a higher computational cost; or we can retrieve it by means of pre-computed look-up tables with different combinations of abundances. As shown in Bressan et al. (2012), this second method is accurate enough and we prefer it for numerical speed reasons. At a given partition of elements (X_i/Z) and metallicity, the tables are divided in two sets: (i) the H-rich set in which there are 10 tables with a varying hydrogen and helium abundances, and (ii) the H-free one composed of 12 tables with a varying helium, carbon, and oxygen composition.

For temperature $\log(T/\text{K}) > 8.5$, we adopt the code described in Timmes & Arnett (1999), because the FREEEOS tables do not include the treatment of pair creation.

2.3 Nuclear reaction network

The nuclear reaction network consists in 72 different reactions and 33 isotopic elements, from hydrogen to zinc. The reaction rates and Q-values are taken from the JINA reaclib database (Cyburt et al. 2010). In the network, we treat all the most important reactions from hydrogen to oxygen burning. The network includes also the reverse reactions of the α -capture. The new adopted reactions with their rates are listed in Table 1. The other reactions, already included in the previous versions of the code, can be found in Table 1 of Fu et al. (2018). In the network, we include all the reactions of the cold-CNO cycle, but not those of the hot-CNO cycle. The latter requires high temperatures (> 0.1 Gk) in H-rich regions to ignite, but these are never reached in our models.

³<http://opalopacity.llnl.gov/>

⁴<http://stev.oapd.inaf.it/aesopus>

⁵<http://freeeos.sourceforge.net/>

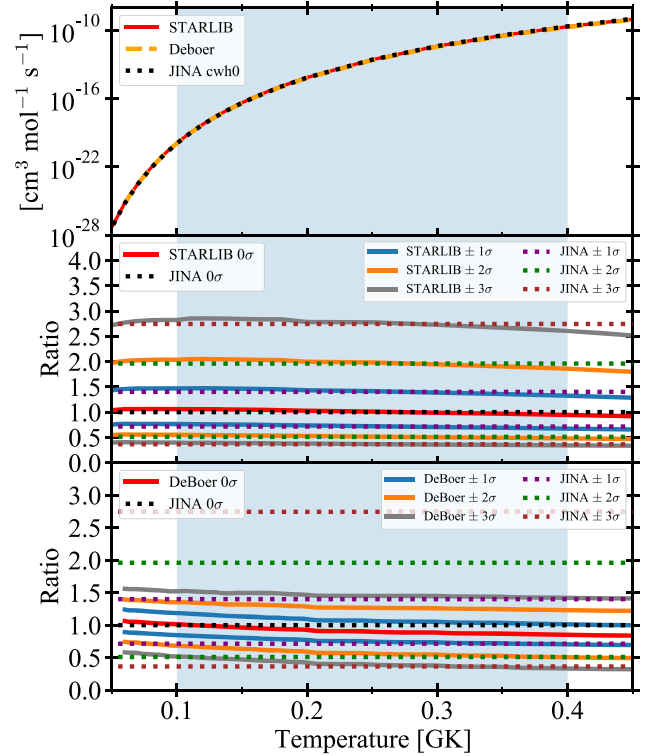


Figure 1. Upper panel: Comparison of the $^{12}\text{C}(\alpha, \gamma)^{16}\text{O}$ rate from STARLIB database, deBoer et al. (2017) and JINA database in red, orange, and black, respectively. The blue shaded area indicates the temperature range of helium burning in the stellar core. Middle panel: Comparison between STARLIB and JINA reaction rates with different σ . All the rates are divided by the standard (0σ) JINA rate. The blue, orange, and grey continuous lines are the STARLIB rates with $\pm 1\sigma$, $\pm 2\sigma$, and $\pm 3\sigma$, respectively. The purple, green, and brown dotted lines indicate the JINA $\pm 1\sigma$, $\pm 2\sigma$, and $\pm 3\sigma$ rates, respectively. Lower panel: Comparison between deBoer et al. (2017) and JINA reaction rates with different σ .

In PARSEC v2.0, nuclear reaction network and element mixing are treated and solved at the same time, adopting an implicit diffusive scheme (more details in Marigo et al. 2013; Costa et al. 2019).

2.4 The $^{12}\text{C}(\alpha, \gamma)^{16}\text{O}$ reaction

For the $^{12}\text{C}(\alpha, \gamma)^{16}\text{O}$ reaction, we use the chw0 (v5) rate from the JINA reaclib database (Fu et al. 2018), which is a re-evaluation of the Buchmann (1996) rate that includes high-lying resonances (Cyburt et al. 2012).⁶

The JINA database does not include uncertainties on the chw0 (v5) rate. To estimate the uncertainties, we compared our adopted rate with the one given in the STARLIB database (Sallaska et al. 2013). In the STARLIB database, each rate is given as a mean value with a correspondent confidence error at 1σ . The $^{12}\text{C}(\alpha, \gamma)^{16}\text{O}$ rate given in the STARLIB database is based on the rate by Kunz et al. (2002).

Fig. 1 shows the comparison of the two rates in the temperature range of the core helium burning, i.e. between about 0.1 and 0.4 Gk. The mean values of the two rates are in agreement within a few percent. To reproduce the uncertainties given by the STARLIB $^{12}\text{C}(\alpha, \gamma)^{16}\text{O}$ reaction rate in the range between -3σ and $+3\sigma$

⁶Relative differences with respect to the most recent JINA reference rate (NACRE, v9) in the temperature range 0.1–0.5 Gk are about 3 per cent.

Table 2. Multiplier factors, f_{CO} , for the $^{12}\text{C}(\alpha, \gamma)^{16}\text{O}$ reaction rates adopted in this work. See text for details.

	$+3\sigma$	$+2\sigma$	$+1\sigma$	0σ	-1σ	-2σ	-3σ
f_{CO}	2.74	1.96	1.4	1.0	0.71	0.51	0.36

we multiplied our adopted JINA rate by a temperature independent multiplier factor, f_{CO} . The values of f_{CO} are listed in Table 2. The middle panel of Fig. 1 shows the ratios of the rates with respect to the JINA standard and at different σ . In the bottom panel of Fig. 1, we also compared the adopted uncertainties with those given by deBoer et al. (2017). We find that the deBoer et al. rates are generally lower than our adopted rates in the case of $+3\sigma$, $+2\sigma$, and $+1\sigma$. In the best value case, the two rates are very similar at low temperature but start to be different at high temperatures. Interestingly, the deBoer et al. rates with -1σ , -2σ , and -3σ show a very similar trend to the STARLIB ones, at temperatures > 0.2 Gk. Hence, had we used the uncertainties from deBoer et al. (2017), our main conclusions on the maximum possible mass of a BH (Section 4.5) would not have changed significantly.

2.5 Pair creation and dynamical instability

The electron-positron creation process may induce dynamical instability during the most advanced phases of massive star evolution. Pair creation absorbs part of the thermal energy of the plasma, consequently lowering the thermal pressure. The plasma is not a perfect gas anymore, and temperature variations do not lead to changes in pressure (Kippenhahn, Weigert & Weiss 2012). Regions in which this process happens become locally dynamically unstable. To check if a star is globally stable or not, a perturbation method should be adopted (Ledoux & Walraven 1958). However, Stothers (1999) showed that an evaluation of the first adiabatic exponent properly weighted and integrated over the whole star, $\langle \Gamma_1 \rangle$, is a very good approximation to determine the dynamical stability of a star. As done by other authors (e.g. Marchant et al. 2019; Farmer et al. 2019, 2020), we adopted the Stothers (1999) stability criterion, which states that a star is stable if

$$\langle \Gamma_1 \rangle = \frac{\int_0^M \frac{\Gamma_1 P}{\rho} dm}{\int_0^M \frac{P}{\rho} dm} > \frac{4}{3}, \quad (4)$$

where Γ_1 is the first adiabatic exponent, P is the pressure, ρ is the density and dm is the element of mass. We decided to compute the above integrals in two ways. In the first case, the integral is calculated from the centre of the star ($M = 0$) up to the mass of helium core ($M = M_{\text{He}}$), defining $\langle \Gamma_1 \rangle_{\text{Core}}$; in the second case, we compute the integral from the centre to the surface of the star ($M = M_{\text{TOT}}$), to include the contribution of the envelope, thus $\langle \Gamma_1 \rangle_{\text{TOT}}$. These two values are computed at each time-step for all tracks. In the case of pure-He stars, $\langle \Gamma_1 \rangle_{\text{Core}} = \langle \Gamma_1 \rangle_{\text{TOT}}$. Since PARSEC is a hydrostatic code, we cannot follow the evolution through the dynamical collapse; we stop the computation if the $\langle \Gamma_1 \rangle < 4/3 + 0.01$, to be conservative, and label the star as a PI. Since we cannot follow the hydrodynamical evolution, we cannot distinguish between PPI and PISN: we classify both of them as PI and we assume that both of them leave no compact object. This makes our results for the BH mass even more conservative, because stars that undergo a PPI might still retain most of their mass after weak pulses and form a massive BH by core collapse (Farmer et al. 2019; Marchant et al. 2019).

To improve the readability of $\langle \Gamma_1 \rangle$ listed in tables, we define the following value $\langle \Gamma_1 \rangle_- \equiv \langle \Gamma_1 \rangle - (4/3 + 0.01)$. When $\langle \Gamma_1 \rangle_- > 0$, we consider the star globally stable, otherwise, the star is unstable. Following the evolution through hydro-dynamical phases is beyond the purpose of this paper.

3 MODELS OF PURE-HE STARS

We first analyse pure-He stars and compare our results with other studies.

3.1 Evolutionary tracks

We computed pure-helium evolutionary tracks with seven different values of the multiplier parameter, f_{CO} , for the $^{12}\text{C}(\alpha, \gamma)^{16}\text{O}$ reaction rate, that correspond to varying the rate between -3σ and $+3\sigma$ (Sallaska et al. 2013). Rotation is neglected in this study, since it increases the CO core and enhances the mass-loss during the evolution, with the effect to lower the final masses (Chatzopoulos & Wheeler 2012; Mapelli et al. 2020; Song et al. 2020). All tracks evolve from the helium ZAMS (He-ZAMS) to core oxygen burning, when stars remain globally stable ($\langle \Gamma_1 \rangle_{\text{TOT}} > 0$).

To build the He-ZAMS, we adopted the same methodology as described by Spera et al. (2019). The new sets are composed of stars with the following masses 20, 30, 40, 50, 55, 60, 65, 70, 80, 90, and 100 M_{\odot} . We adopted the solar-scaled element mixture by Caffau et al. (2011), and a metallicity of $Z = 0.001$. We choose this particular value of metallicity to better compare our results with those found by Farmer et al. (2019), Farmer et al. (2020). For the mixing treatment, we adopt the mixing length theory (MLT, Böhm-Vitense 1958) with a fixed solar calibrated value of the mixing length, $\alpha_{\text{MLT}} = 1.74$ (Bressan et al. 2012). We adopt the Schwarzschild criterion to define the convective regions, and a core overshooting with a mean free path of the convective element across the border of the unstable region of $\lambda_{\text{ov}} = 0.4$ in units of pressure scale height, H_p . Therefore, we are assuming an overshooting distance of $\approx 0.2 H_p$ above the convective core (Costa et al. 2019).

In the convective envelope, we adopt an undershooting distance of $\Lambda_{\text{env}} = 0.7 H_p$ below the border of the unstable region. This value of Λ_{env} is calibrated on observations. In particular, it allows us to reproduce the location of the red giant branch (RGB) bumps and their luminosity function, and the extension of blue loops of intermediate-mass stars, in colour-magnitude diagrams of globular clusters (Alongi et al. 1991; Tang et al. 2014; Fu et al. 2018). Tang et al. (2014) showed that higher values of Λ_{env} might be needed in order to better reproduce the observed blue-to-red supergiants ratios in low metallicity dwarf irregular galaxies, while (Fu et al. 2018) suggested that an even higher value should be used to fit the RGB bumps of the most metal poor globular clusters.

Fig. 2 shows the evolution of three selected sets computed with f_{CO} corresponding to $+3\sigma$, 0σ , and -3σ . Stars begin their evolution from the He-ZAMS. We define such phase as the moment in which the star is fully sustained by the nuclear reactions' energy, and the star has burnt less than 1 per cent of the helium hosted in the core. During the helium main sequence (He-MS), all stars evolve to higher luminosity. Stars with $M_{\text{ZAMS}} < 50 M_{\odot}$ evolve directly toward hotter effective temperatures. Stars with $M_{\text{ZAMS}} \geq 50 M_{\odot}$ first expand reducing their effective temperature and then turn to higher temperatures. As the evolution proceeds, the stars move to higher luminosity and hotter effective temperature and start to burn and deplete sequentially carbon, neon, and then oxygen in their cores.

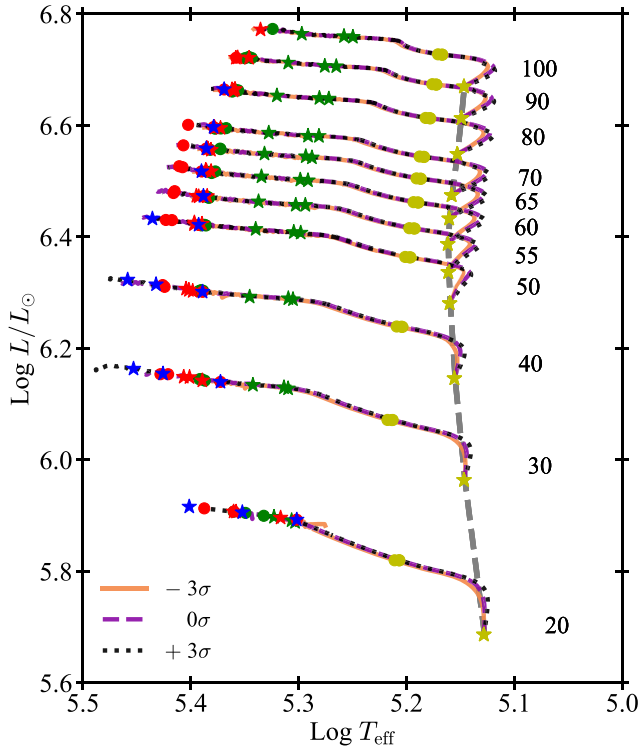


Figure 2. HR diagram of three sets of tracks of pure-He stars, computed with $Z = 0.001$. Solid black lines, dashed green lines and dotted brown lines indicate tracks computed with the $^{12}\text{C}(\alpha, \gamma)^{16}\text{O}$ reaction rate -3σ , with 0σ and with $+3\sigma$, respectively. The dashed grey line shows the pure He-ZAMS. The symbols indicate helium (yellow), carbon (green), neon (red), and oxygen (blue) burning phases, respectively. Stars and circles symbols indicate the ignition and depletion of each element, respectively. The numbers on the right of the ZAMS line indicate the initial mass in M_{\odot} units.

Fig. 2 shows that different rates do not affect the path followed by stars in the HR-diagram, but instead they may affect when and where stars ignite and deplete carbon, neon and oxygen in their cores. These small variations are due to different mass fractions of carbon and oxygen present in the cores at the end of the He-MS, that depend on the assumed rate of the $^{12}\text{C}(\alpha, \gamma)^{16}\text{O}$ reaction. The evolution is eventually stopped if the star becomes globally unstable by checking the $\langle \Gamma_1 \rangle_{\text{TOT}}$ value defined in equation (4). In the other case, we continue the evolution until the lowest possible value of central oxygen is reached. These values are shown in Table A1. At this point, we stop the evolution because the evolutionary times become too short and induce numerical instabilities in the code.

Fig. 3 shows the duration of the He-MS and the resulting mass of the CO core, M_{CO} , divided by the M_{CO} of the star with 0σ , as a function of the initial mass, $M_{\text{He-ZAMS}}$, and for different reaction rates. Looking at the same initial mass, models computed with higher rates have slightly longer He-MS than models with lower rates. On the other hand, the M_{CO} is almost not affected by the different rates adopted, and the differences are below the 1 per cent in the worst case (as shown in the central panel). The main difference at the end of the He-MS between models computed with different rates is the carbon-to-oxygen ratio in the CO core, that is shown in the bottom panel. In the case of the $20M_{\odot}$ stars, we find the largest variation, that goes from 1 (i.e. the CO core is composed 50 per cent of ^{12}C and

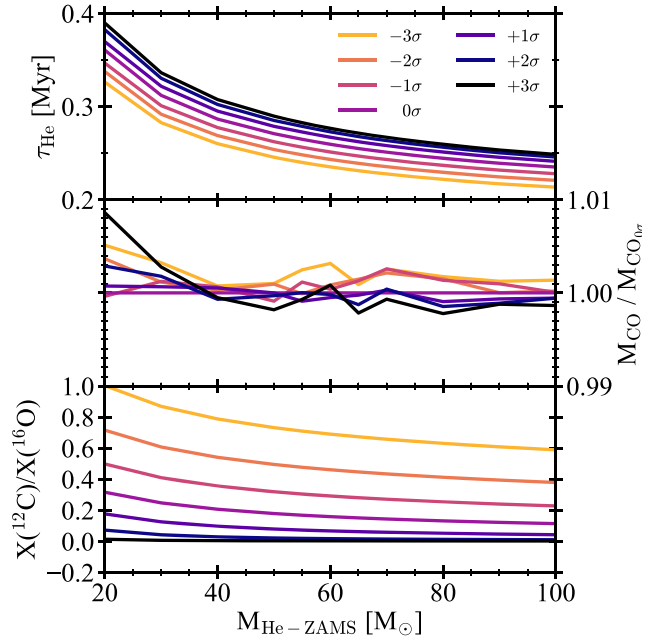


Figure 3. Upper panel: He-MS lifetimes versus the initial mass of pure-He stars for different adopted rates. Middle panel: Ratio between the CO core masses and the CO core mass of the model computed with 0σ at the end of the He-MS. Lower panel: carbon-to-oxygen ratio in the CO cores at the end of the He-MS.

50 per cent of ^{16}O) to about 0.01 (i.e. the CO core is almost totally composed of ^{16}O).

To show the main differences on the evolution of our pure-He stars due to different assumed rates, in Fig. 4 we plot the Kippenhahn diagrams of pure-He stars with $M_{\text{ZAMS}} = 40 M_{\odot}$ with different rates. The mass lost by the star through the evolution is just about $1.2 M_{\odot}$, and is mainly lost during the He-MS. During the He-MS, these stars build up massive convective cores that mix the star up to the 92 per cent of the entire mass. Different rates slightly affect both the luminosity of the model and the size of the convective core leading to relative differences of He-MS lifetimes up to 18 per cent between the model computed with $+3\sigma$ and the one with -3σ (appreciable also in Fig. 3).

After the He-MS, stars are totally radiative and have massive CO cores that do not change much depending on the assumed rate of the $^{12}\text{C}(\alpha, \gamma)^{16}\text{O}$ reaction, as shown in Fig. 3. On the other hand, the carbon-to-oxygen ratio is very different. The carbon (oxygen) mass fraction in the CO core are 0.43, 0.17, and ≈ 0.004 (0.52, 0.79, and 0.91) for stars with -3σ , 0σ , and with $+3\sigma$, respectively. Up to this stage, the evolution of these three models is quite similar.

Stars ignite carbon in their centre when temperatures reach 0.8–1 GK. The carbon burning phase lasts for about 21 years in the case of the -3σ model, 10 years and 5 years for models with 0σ and $+3\sigma$, respectively. During this phase, a helium burning shell forms above the CO core. The neon burning starts when the central temperatures are about 1.4 GK and all the neon in the central parts of the star is depleted in about 46, 6, and 2 days for models computed with -3σ , 0σ , and $+3\sigma$, respectively. During this phase, depending on the carbon mass fraction in the CO core, models may turn-on a carbon burning shell above the centre of the star, which develops a big intermediate convective region in the CO core. Such convective region may lead to a growth of

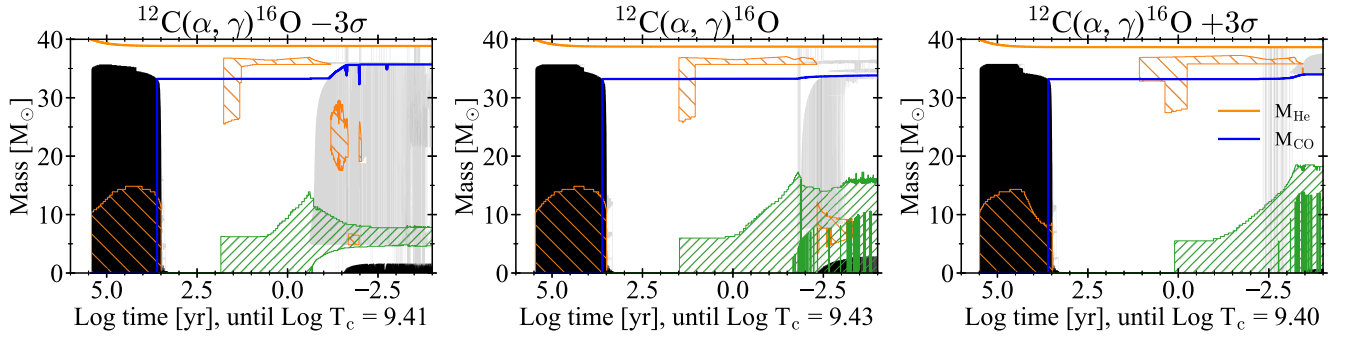


Figure 4. Kippenhahn diagrams of three models of pure-He stars with $M_{\text{ZAMS}} = 40 M_{\odot}$ and with the $^{12}\text{C}(\alpha, \gamma)^{16}\text{O}$ reaction rate -3σ , 0σ , and with $+3\sigma$ in the left-hand, middle and right-hand panels, respectively. The black areas represent the convective unstable core, while the grey areas indicate the convective envelope or intermediate convective regions between the core and the surface of the star. Continuous yellow and blue lines show the stellar mass and the CO core. The yellow and green hatched areas indicate the helium and carbon burning regions, respectively. We plot zones that contribute at least for the 1 per cent of the L_{He} and L_{C} luminosity at a given time-step.

the CO core, and provides fresh carbon to the C-burning shell. The energy released by the off-centre carbon burning sustains the external layers of the star, and avoids the stellar collapse due to the pair creation instability. The important role of the convective C-burning shell in preventing the collapse has been reported by other authors (such as Takahashi 2018; Farmer et al. 2020).

Finally, oxygen burning takes place at the centre of the star when the central temperature reaches ≈ 2 GK. At this point of the evolution, only the model computed with -3σ is globally stable and we can follow the evolution until oxygen’s depletion. The model with the 0σ becomes dynamically unstable at about half of the oxygen burning, while the one with $+3\sigma$ becomes dynamically unstable at the beginning of oxygen burning. The large amount of energy released by oxygen burning generates a small convective core of about $1.63 M_{\odot}$, $2.87 M_{\odot}$, and $0.83 M_{\odot}$ at the end of the computation for models with -3σ , 0σ , and $+3\sigma$, respectively. If possible, all the oxygen is depleted leaving a core mainly composed of silicon and sulfur. The model with -3σ burns the oxygen in about 30 days. At this point, the -3σ model is near to silicon burning and to the final core collapse.

Fig. 5 shows the evolution of the $\langle \Gamma_1 \rangle_{\text{TOT}}$ value of pure-He stars’ models with $M_{\text{ZAMS}} = 40 M_{\odot}$ with different rates adopted for the $^{12}\text{C}(\alpha, \gamma)^{16}\text{O}$ reaction. This figure shows the evolution from the ignition of carbon. As already seen in Fig. 4, our models start to behave differently after carbon depletion from the core, depending on the amount of carbon-to-oxygen ratio in their CO cores. Models with f_{CO} corresponding to $^{12}\text{C}(\alpha, \gamma)^{16}\text{O}$ rates between 0σ and $+3\sigma$ become more and more unstable as they evolve. In contrast, models with -1σ , -2σ , and -3σ tend to stabilize and continue their evolution until oxygen depletion, avoiding PI.

3.2 Pre-supernova masses

Table A1 in Appendix A shows the properties of the pure-He stars computed in this work. The final fate is assigned as follows: when $\langle \Gamma_1 \rangle_{\text{TOT-}} > 0$, the star is stable, continues to evolve through the last burning phases and a final core collapse (CC) will form a black hole with mass $\leq M_{\text{Pre}}$. When $\langle \Gamma_1 \rangle_{\text{TOT-}} \leq 0$, the star is dynamically unstable. Depending on its mass, it may start to pulsate losing mass through PPI, or it might explode after a single pulse, becoming a PISN and leaving no remnant. In Table A1, we refer to both PPI and

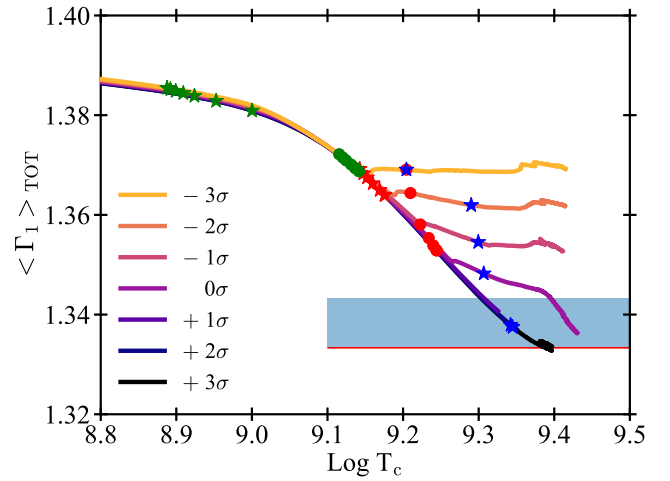


Figure 5. Comparison of the averaged first adiabatic exponent, $\langle \Gamma_1 \rangle_{\text{TOT}}$ versus the central temperature of pure-He stars models with $M_{\text{ZAMS}} = 40 M_{\odot}$. The plot shows the final phases at the end of the evolution. Coloured lines indicate models computed with different $^{12}\text{C}(\alpha, \gamma)^{16}\text{O}$ reaction rates. Symbols indicate the start and the end of core burning phases of elements with the same colour code as adopted in Fig. 2. The red horizontal line corresponds to $\langle \Gamma_1 \rangle = 4/3$. The blue shaded area indicates values between $4/3$ and $4/3 + 0.01$, range in which the whole star starts to be dynamically unstable.

PISN as PI. The evolution through such phases must be followed by means of hydro-dynamical simulations, as done by, e.g. Woosley (2017), Takahashi (2018) and Marchant et al. (2019). Since we did not run hydro-dynamical simulations, we conservatively assume that both stars going through PPI and stars undergoing PISN leave no compact objects. Hence, we will obtain lower limits to the maximum compact object mass.

In Appendix B, we show a comparison between our pure-He star models and those computed by Farmer et al. (2020) with the MESA stellar evolutionary code (Paxton et al. 2011, 2013, 2015, 2018). From such a comparison we see that our stable models at the end of the computation are very similar to the models of Farmer et al. (2020) that are dynamically stable during the oxygen burning phase, which evolve directly toward the final CC.

Due to both the low metallicity adopted, that leads to mass-loss rates of $\approx 5 \times 10^{-6} M_{\odot} \text{yr}^{-1}$, and to the short lifetimes of pure-He

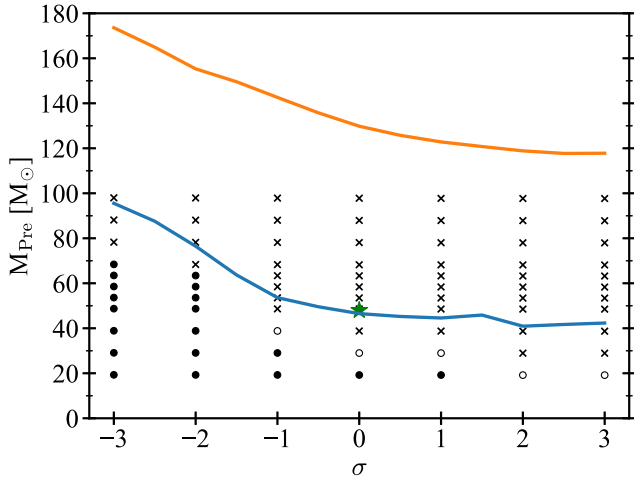


Figure 6. Pre-Supernova masses of pure-He stars as a function of the $^{12}\text{C}(\alpha, \gamma)^{16}\text{O}$ reaction rate. Circles indicate models that are dynamically stable while burning oxygen. Empty circles: models with a central oxygen mass fraction between 0.3 and 0.2; filled circles: models with a central oxygen mass fraction lower than 0.2. Black crosses indicate models that are dynamically unstable (i.e. $\langle \Gamma_1 \rangle_{\text{TOT}} < 0$). Table A1 lists all the values plotted here. Continuous blue and orange lines indicate the lower and higher mass gap edges by Farmer et al. (2020), respectively. The green star at 0σ indicate the $M_{\text{Gap}} = 48 M_{\odot}$ found by Woosley (2017) for pure-He stars.

stars, of the order of 10^5 yr, all the pure-He models computed have pre-supernova masses, M_{Pre} , very close to $M_{\text{He-ZAMS}}$. As discussed before and also shown in Fig. 3, different rates for the $^{12}\text{C}(\alpha, \gamma)^{16}\text{O}$ reaction change the carbon-to-oxygen mass fraction at the end of the He-MS, but do not influence the He and CO core mass.

Fig. 6 shows the lower edge of the PI gap as a function of the $^{12}\text{C}(\alpha, \gamma)^{16}\text{O}$ reaction rate. For pure-He stars, the maximum He-ZAMS mass that results in a stable model and evolves until core collapse is about 68 and 19 M_{\odot} , in the case of $^{12}\text{C}(\alpha, \gamma)^{16}\text{O}$ reaction rates -3σ and $+3\sigma$, respectively. This trend is similar to the one shown by Farmer et al. (2020), but in our case the maximum mass is always lower by $\approx 10\text{--}20 M_{\odot}$ than theirs, for each assumed rate. This happens because, on the one hand, PARSEC includes slightly different physical prescriptions for the computation of the evolutionary tracks (e.g. for the opacity, mass-loss, and convection treatment) and, on the other hand, we do not compute the hydro-dynamical evolution of the models after they become unstable. Hence, we conservatively assume that all stars with $\langle \Gamma_1 \rangle \leq 0$ leave no compact object, because we cannot distinguish between PPI and PISN and we cannot model mass loss during PPI. Hydro-dynamical simulations of PPI (Marchant et al. 2019; Farmer et al. 2020) show that, depending on the mass of the star, the pulses may eject just few tenths of M_{\odot} before the star stabilizes. After this small mass-loss, the star continues its evolution until core collapse. Hence, including hydrodynamical evolution might stabilize some of our models and lead to a higher value of the M_{Gap} . For the same reason, our maximum BH mass obtained adopting the standard $^{12}\text{C}(\alpha, \gamma)^{16}\text{O}$ rate differs by $\approx 20 M_{\odot}$ with respect to the maximum BH mass obtained from pure-He stars by Woosley (2017), that is 48 M_{\odot} , and by Leung et al. (2019), 50 M_{\odot} .

The analysis of pure-helium stars, the comparison with Farmer et al. (2020) pure-He models (Appendix B), and the fact that our results are comparable to previous work confirm that our criterion for stability is a conservative one to decide whether a stellar model is stable, even if we do not follow the hydrodynamical evolution of

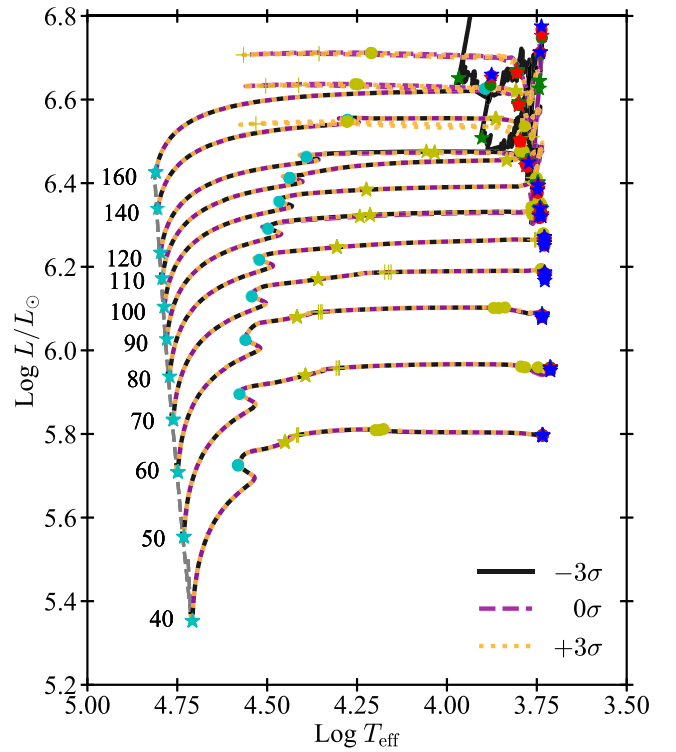


Figure 7. HR diagram of the three sets of H stars computed with $Z = 0.0003$ and with different reaction rates. The colour code of lines and symbols is the same as in Fig. 2. The cyan stars (circles) indicate the beginning (the end) of the hydrogen burning phase. The grey dashed line is the ZAMS. The numbers on the left of the ZAMS are the values of M_{ZAMS} in units of M_{\odot} .

the final stages. Since we do not follow the evolution through the pulsation PPI phase, our results are lower limits to the M_{Gap} .

4 FULL STELLAR MODELS WITH HYDROGEN ENVELOPE

We now consider stellar models with hydrogen envelopes, computed with the same version of PARSEC as described in Section 3.1. Grids of evolutionary tracks are calculated with different values of the multiplier parameter, f_{CO} , as shown in Table 1.

4.1 Evolutionary tracks

Each grid contains stellar models with initial masses of 40, 50, 60, 70, 75, 80, 85, 90, 95, 100, 105, 110, 120, 140, and 160 M_{\odot} . Our models begin their evolution from the ZAMS and evolve until the end of the central oxygen burning, when possible. The initial metallicity and helium content are $Z = 0.0003$ and $Y = 0.249$, respectively (Bressan et al. 2012).

In Fig. 7, we plot the HR diagram of three selected sets of tracks computed with f_{CO} corresponding to $+3\sigma$, 0σ , -3σ . The $^{12}\text{C}(\alpha, \gamma)^{16}\text{O}$ reaction does not affect the hydrogen burning phase and the models with the same mass evolve in the same way during the MS.

After the MS, the stellar cores rapidly contract until their central temperature is high enough for helium ignition. Stars cross the so called Hertzsprung gap while the effective temperatures decrease. Whether a massive star ignites helium as blue supergiant (BSG) or as a yellow/red supergiant (YSG/RSG) star depends on many stellar

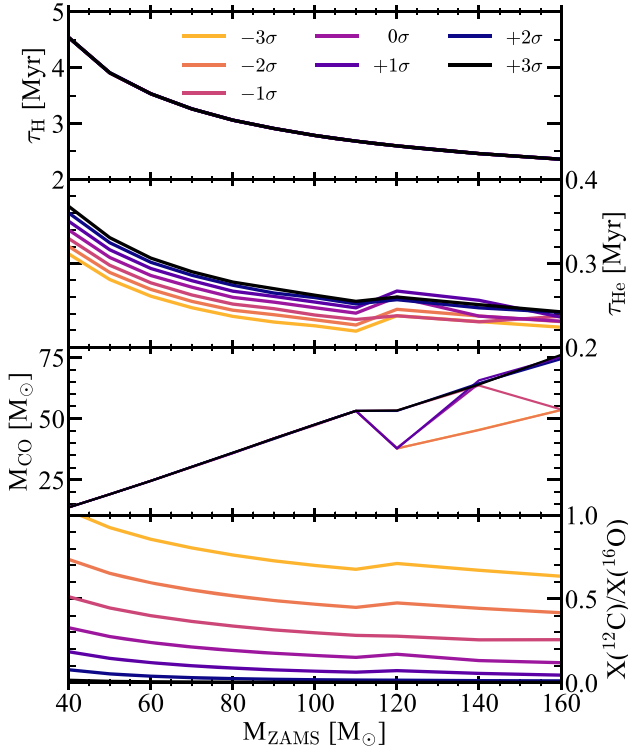


Figure 8. Same as Fig. 3, but for stars with hydrogen envelopes. The upper panel shows the MS lifetimes of hydrogen stars versus the ZAMS mass. The second panel from the top shows the CHeB lifetimes. The third panel shows the CO core mass. Different colours indicate different $^{12}\text{C}(\alpha, \gamma)^{16}\text{O}$ rates (several of these lines overlap). Table A2 lists all the relevant quantities. The lower panel shows the carbon-to-oxygen ratio in the CO cores at the end of CHeB.

and physical parameters (such as the stellar mass, the metallicity, the mass-loss, the opacity, and previous mixing efficiency). In our sample, all models with $M_{\text{ZAMS}} \leq 90 M_{\odot}$ ignite helium as BSG stars, while more massive ones ignite helium as YSG/RSG stars.

During the CHeB, stars develop a convective core that stops growing when the central He mass fraction falls below ≈ 0.5 . In this phase, the carbon fraction initially increases up to a maximum and then decreases because of the effects of the $^{12}\text{C}(\alpha, \gamma)^{16}\text{O}$ reaction. As the $^{12}\text{C}(\alpha, \gamma)^{16}\text{O}$ rate increases (from -3σ to $+3\sigma$), more carbon is converted into oxygen, eventually leaving an almost carbon-free core at the end of the CHeB phase in the case of the model computed with $+3\sigma$. However, these differences do not affect much the CHeB lifetimes and the mass of the CO core, as shown in Fig. 8. During the CHeB, the star develops several intermediate convective regions in the envelope, that remain detached from the He core for the remaining evolution. As shown in Fig. 8, the CHeB lifetimes are only slightly affected by the assumption of different f_{CO} values, with a maximum difference of $\approx 5 \times 10^4$ yr in the case of the $M_{\text{ZAMS}} = 40 M_{\odot}$ star. Moreover, adopting different f_{CO} values has no impact on the CO core masses left after the CHeB phase. Only in stars with $M_{\text{ZAMS}} \geq 120 M_{\odot}$ the $^{12}\text{C}(\alpha, \gamma)^{16}\text{O}$ rate does affect the CO mass, because of the presence of an efficient envelope undershooting, as it will be further discussed in Section 4.3. Fig. 8 shows that the major effect of changing f_{CO} is on the central carbon-to-oxygen ratio left at the end of the CHeB, as in pure-He stars.

At such low metallicity, all our models evolve through advanced burning phases as RSG stars. This is due to the low stellar winds that allow stars to keep their massive H-rich envelope.

After the CHeB phase, the core starts to contract again increasing its density and temperature. Meanwhile, neutrino losses tend to cool down the core, but, when the central temperature reaches ≈ 1 GK, carbon is ignited. Stars computed with lower $^{12}\text{C}(\alpha, \gamma)^{16}\text{O}$ rates have longer lifetimes than models computed with higher $^{12}\text{C}(\alpha, \gamma)^{16}\text{O}$ rates.

After carbon depletion, neon photo-disintegration begins at the stellar centre when the temperature rises up to about 1.2–1.5 GK. During carbon and neon burning, our models have radiative cores and convective envelopes. As already seen for pure-He stars, during the central neon burning phase, carbon burns off-centre in a shell that, in case of low $^{12}\text{C}(\alpha, \gamma)^{16}\text{O}$ rates, is able to turn on an intermediate convective region.

This convective zone inside the CO core continuously provides fresh carbon to the burning shell that sustains the overlying layers, thus delaying the ignition of oxygen in the core. As the evolution proceeds further, $\langle \Gamma_1 \rangle_{\text{TOT}}$ may become lower than $4/3 + 0.01$, indicating that the star becomes globally unstable. In this case, the computation is stopped. Otherwise, we continue the evolution until the end of central oxygen burning, when eventually the code encounters some convergence problems. Apart from a few isolated cases, the values of the final central oxygen mass fractions in stable models are between 0.01 and 0.3 (Table A2).

After the central oxygen burning phase, the evolution of the core and of the envelope become decoupled. Therefore, in analogy with the pure-He models, we can assume that if the star remains dynamically stable during the core oxygen burning, it will evolve towards the advanced silicon and iron burning phases and finally, to the core collapse.

Fig. 9 shows the Kippenhahn diagrams of stars with $M_{\text{ZAMS}} = 100 M_{\odot}$ computed with f_{CO} corresponding to $^{12}\text{C}(\alpha, \gamma)^{16}\text{O}$ rate $+3\sigma$, 0σ , and -3σ . The three models evolve in a similar way during the MS and the CHeB phases. They build up a convective core that decreases over time in the MS. At the end of the MS, stars have an He core of $\approx 50 M_{\odot}$. During the CHeB, the models develop a convective core of $\approx 47 M_{\odot}$, in which all the helium is converted to carbon, oxygen, and neon.

When temperature and density are high enough, carbon is ignited in the core. It burns for 12 yr, 2.8 yr, and only 4 months in the case of models computed with f_{CO} corresponding to -3σ , 0 and $+3\sigma$, respectively. After the carbon burning, neon photo-disintegration takes place in the star centre, and it lasts for about 20, 2, and 1.4 days for models computed with -3σ , 0 , and $+3\sigma$, respectively. At this point, only the model computed with -3σ remains globally stable and burns central oxygen in a small convective core of about $2 M_{\odot}$. At the end of the computation, this $2 M_{\odot}$ core is composed of 15 per cent ^{16}O , 45 per cent ^{28}Si , 30 per cent ^{32}S , and 10 per cent heavier elements. This star will continue its evolution through the most advanced burning phases and then will collapse forming a BH. The other models computed with 0σ and $+3\sigma$ do not have sufficient ^{12}C in the CO core to prevent PI, hence they become unstable before the ignition of oxygen.

Fig. 10 shows the evolution of the averaged first adiabatic exponent, $\langle \Gamma_1 \rangle_{\text{TOT}}$, of the models with $100 M_{\odot}$ and computed with different $^{12}\text{C}(\alpha, \gamma)^{16}\text{O}$ rates. Depending on the assumed rate, the star enters or not in the unstable regime. In this case, only models with -3σ and -2σ remain stable during the oxygen burning phase. The other models become unstable shortly after the end of the neon burning phase.

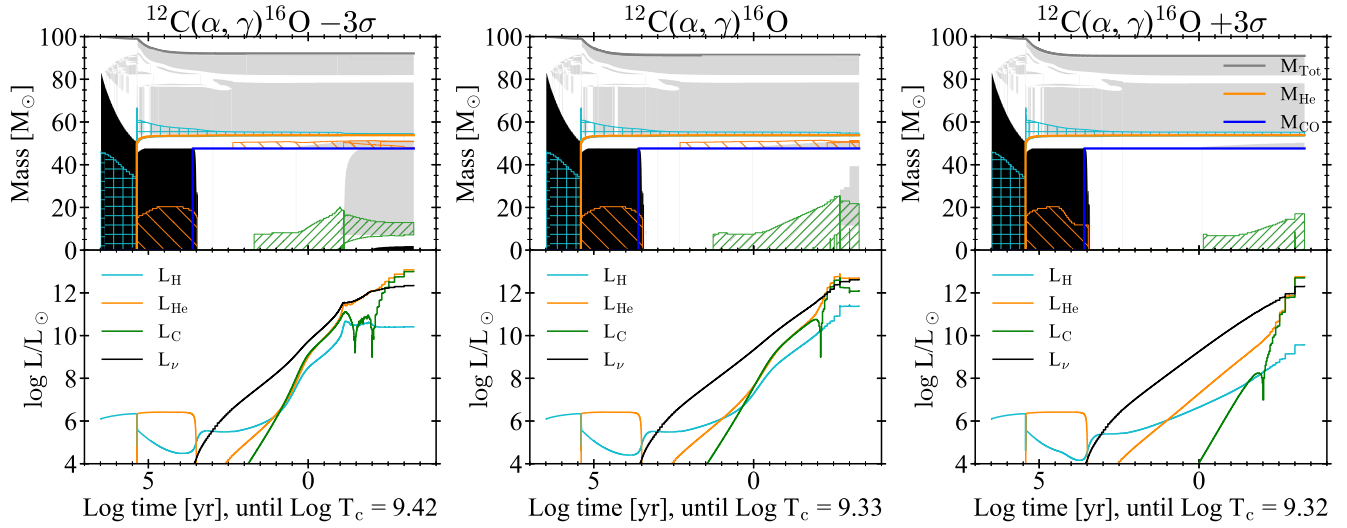


Figure 9. Upper panels: Same as Fig. 4, but for hydrogen stars with $M_{\text{ZAMS}} = 100 M_{\odot}$. The continuous grey lines indicate the total stellar mass. The cyan-coloured areas indicate the hydrogen burning regions, which contribute at least for the 1 per cent of the L_{H} . Lower panels: Luminosity as a function of time from H-burning, He-burning, C-burning, and neutrinos in cyan, orange, green, and black, respectively.

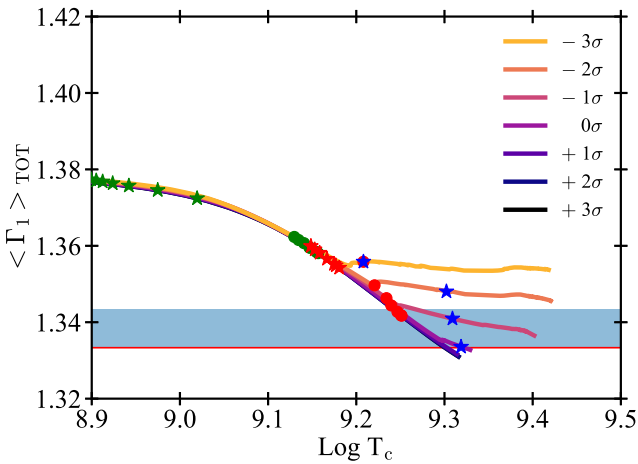


Figure 10. Comparison of the $\langle \Gamma_1 \rangle_{\text{TOT}}$ values versus the central temperature of stars with hydrogen envelopes and $M_{\text{ZAMS}} = 100 M_{\odot}$. Here, we use the same colour code for lines and symbols as in Fig. 5. The lines corresponding to $+2$ and $+3 \sigma$ are barely visible, because they almost perfectly overlap with the $+1 \sigma$ line.

4.2 Pre-supernova masses

Table A2 in Appendix A shows the results for the stars with H envelopes. The columns list the same quantities as shown in Table A1, with the exception of the first adiabatic exponent (defined in Section 2.5), that here is computed in two ways: (i) for whole star, $\langle \Gamma_1 \rangle_{\text{TOT}} = \langle \Gamma_1 \rangle_{\text{TOT}} - (4/3 + 0.01)$, and (ii) for the He core, $\langle \Gamma_1 \rangle_{\text{Core}} = \langle \Gamma_1 \rangle_{\text{Core}} - (4/3 + 0.01)$. We find that $\langle \Gamma_1 \rangle_{\text{Core}}$ is always slightly lower than $\langle \Gamma_1 \rangle_{\text{TOT}}$. The envelope of massive stars could be near the dynamical instability too, depending on the ionization state of the plasma (Stothers 1999). $\langle \Gamma_1 \rangle_{\text{Core}}$ and $\langle \Gamma_1 \rangle_{\text{TOT}}$ are not significantly different, because $\langle \Gamma_1 \rangle$ is a weighted integral and the external parts of the envelope contribute less than the internal parts of the star. We use the same methodology adopted for the pure-He stars to assign the final fate of stars. In the case of $\langle \Gamma_1 \rangle_{\text{TOT}} > 0$, the star is considered globally stable and evolves until the final CC. On the other hand,

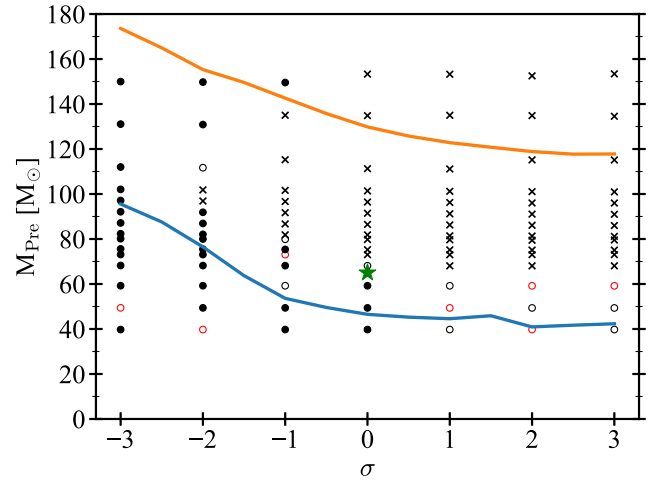


Figure 11. Pre-supernova masses as a function of the $^{12}\text{C}(\alpha, \gamma)^{16}\text{O}$ reaction rate for stars with H envelopes. Circles indicate models that are dynamically stable while burning oxygen. Red empty circles: Models with a central oxygen mass fraction higher than 0.3. Black empty circles: Models with a central oxygen mass fraction between 0.3 and 0.2. Filled circles: Models with a central oxygen mass fraction lower than 0.2. Black crosses indicate models that are dynamically unstable (i.e. $\langle \Gamma_1 \rangle_{\text{TOT}} < 0$). The PI mass gap is completely filled in the -3σ case, because of the effect of the dredge-up (see Section 4.2 for details). Continuous blue and orange lines indicate the lower and higher mass gap edges by Farmer et al. (2020), respectively. The green star at 0σ indicates the $M_{\text{gap}} = 65 M_{\odot}$ found by Woosley (2017) for stars with hydrogen envelope.

if $\langle \Gamma_1 \rangle_{\text{TOT}} \leq 0$, the star becomes dynamically unstable and the PI-induced collapse leads to a PPI or a PISN. This fate is indicated with the label PI in the Table. We find that the final fate does not change if we assume $\langle \Gamma_1 \rangle_{\text{TOT}}$ or $\langle \Gamma_1 \rangle_{\text{Core}}$.

Fig. 11 shows the pre-supernova masses of stars with H envelope as a function of the $^{12}\text{C}(\alpha, \gamma)^{16}\text{O}$ rate. The lower edge of the mass gap (M_{gap}) ranges from ≈ 60 to $\approx 92 M_{\odot}$ in the case of models computed with $+3 \sigma$ and -2σ , respectively. Interestingly, we find no mass gap in the case of models computed with -3σ . The maximum M_{Pre} is

$\approx 150 M_{\odot}$. Moreover, we find that stars computed with -2σ and with initial masses of 140 and 160 M_{\odot} do not become unstable and burn oxygen non-explosively, with final M_{Pre} masses of ≈ 131 and $\approx 150 M_{\odot}$ respectively.

The disappearance of the mass gap for models with -3σ is due to a dredge-up during the CHeB, that reduces the mass of the CO core with the effect of stabilizing the core. This process is described in detail below.

In this case, the lower edge of the PI window is higher than that found by Farmer et al. (2020), because we consider stars that still have their hydrogen envelopes. The range of maximum masses we find is in agreement with the maximum BH mass $\approx 65 M_{\odot}$, found by Woosley (2017) for stars with hydrogen envelope, and overlaps with the range obtained by Takahashi (2018), that is between 100 and 270 M_{\odot} .

4.3 Envelope undershooting and dredge-up during the advanced phases

The dredge-up is an opacity-driven process that begins when the star approaches the location of RSG. The envelope expands and cools, the opacity rises, and the radiative temperature gradient becomes superadiabatic in the inner envelope layers. As a consequence, the base of the convective envelope extends inwards, crossing the H-He discontinuity, and deepening into the He core (envelope undershooting).

As described in Section 3.1, in PARSEC we adopt the undershooting at the bottom of the outermost convective region. As a consequence, only models that develop fully convective envelopes, extending from the surface to the He core, undergo the dredge-up.

Models with $M_{\text{ZAMS}} < 120 M_{\odot}$, ignite and deplete helium as BSG/YSG stars (Fig. 7), regardless of the $^{12}\text{C}(\alpha, \gamma)^{16}\text{O}$ reaction rate assumed. Such models show a complex structure with many intermediate convective regions: they do not develop fully convective envelopes and avoid the dredge-up (see Fig. 9).

In contrast, all our models with $M_{\text{ZAMS}} \geq 120 M_{\odot}$ become RSG stars after the MS, regardless of their $^{12}\text{C}(\alpha, \gamma)^{16}\text{O}$ rate. They develop a large convective envelope and undergo a dredge-up after the ignition of helium, which extracts a few M_{\odot} of material from the core (Fig. 12).

In the following stages, models with high $^{12}\text{C}(\alpha, \gamma)^{16}\text{O}$ rates have a very different evolution from models with low $^{12}\text{C}(\alpha, \gamma)^{16}\text{O}$ rates (Fig. 12). Models with high $^{12}\text{C}(\alpha, \gamma)^{16}\text{O}$ rates tend to perform blue loops, as in the case of less massive stars (Iben 1974; Bertelli, Bressan & Chiosi 1985; Brunish & Becker 1990). For example, the 140 M_{\odot} model with $+3\sigma$ $^{12}\text{C}(\alpha, \gamma)^{16}\text{O}$ rate begins the blue loop when the $^{12}\text{C}(\alpha, \gamma)^{16}\text{O}$ luminosity exceeds the triple- α one. At higher effective temperatures, the H-burning shell re-ignites and the convective envelope becomes thinner, while some detached intermediate convective zones appear (left-hand panels of Fig. 12). Envelope undershooting is not applied to such intermediate convective regions. Thus, the penetration into the He-core is not boosted even if, sometimes, convection extends down to the bottom of the H-rich envelope. We will investigate these cases in a follow-up study.

In contrast, models computed with low $^{12}\text{C}(\alpha, \gamma)^{16}\text{O}$ reaction rates deplete He in the RSG branch, maintaining their large convective envelopes. Hence, the dredge-up process continues (right-hand panels of Fig. 12), leading to a significant decrease of the He core mass during CHeB. This keeps these models out of the PI regime.

Fig. 13 shows the complete Kippenhahn diagram and the luminosity evolution until the end of the O-burning of a star with $M_{\text{ZAMS}} = 140 M_{\odot}$ and $^{12}\text{C}(\alpha, \gamma)^{16}\text{O}$ rate -3σ . During the MS, the star has

a big convective core, which decreases over time, and a radiative envelope. As the core recedes, small intermediate convective zones form in the envelope. At the end of the MS, the star moves towards the red part of the HR-diagram expanding and cooling. At the beginning of the CHeB, the star develops a large convective region that, after about 5×10^4 yr, extends from the stellar surface to the bottom of the H-rich envelope (upper-right panel of Fig. 12). During this phase, the H-burning shell quenches out and the undershooting at the base of the envelope penetrates in the He core bringing helium up to the surface (dredge-up).

During CHeB phase, more than $\approx 20 M_{\odot}$ of helium are extracted from the core (Table A2). The temperature at the bottom of the H-burning shell (T_b) reaches 40 Mk. At the end of this stage, the envelope is He-rich (with an helium mass fraction of 0.52) and has super-solar metallicity ($Z_{\text{CNO}} \approx 0.13$).

After CHeB, the core contracts and the H-shell ignites again, being the only nuclear energy source for a while. The excess luminosity causes a further quick penetration of the external convection corresponding to a second dredge-up. This brings the H discontinuity very close to the CO core leaving only a very thin He shell. In the meantime, the core contracts and both neutrino and hydrogen luminosities rise. The latter causes a further expansion of the external envelope accompanied by a continuous convective envelope undershooting into the CO core. T_b reaches about 70 MK. The undershooting mixing and subsequent hot bottom burning continue until carbon ignites in the centre, increasing appreciably the surface metallicity. At this stage, the convective envelope has a mass of $\approx 105 M_{\odot}$ and a composition of 3.5 per cent ^1H , 23 per cent ^4He , 48 per cent ^{14}N , 23 per cent ^{16}O , and 2.5 per cent of ^{20}Ne and heavier elements. At the end of the central carbon burning phase, lasting for 5.7×10^2 yr, the CO core mass is $\approx 24.8 M_{\odot}$. Subsequent central neon burning lasts for about 2 months, while carbon burns in a shell above the core.

At this point, the star, which is well outside the PI region, evolves through the advanced burning phases until core collapse. This is shown in Fig. 14 where the upper panel shows the $(\Gamma_1)_{\text{TOT}}$ value as a function of the central temperature, while the lower one shows the evolution of the central density and temperature. These plots show models with $M_{\text{ZAMS}} = 140 M_{\odot}$ computed with different $^{12}\text{C}(\alpha, \gamma)^{16}\text{O}$ reaction rates. The branching moment between models happens just after the beginning of the CHeB, when stars with rate -3σ and -2σ undergo the dredge-up, which erodes significantly the He core. The model with -3σ has a second branching, when the dredge-up starts to extract matter from the CO core. The -2σ model does not undergo this second branching. In all the other cases, the star evolves becoming unstable during or shortly after the neon burning phase in the core.

Table A2 shows if a star undergoes the dredge-up during its evolution. It is worth to note that not all the stars that experience the dredge-up avoid the PI.

4.4 Comparison with previous works

Takahashi (2018) found that very massive stars avoid pulsational PI if they develop a carbon burning shell in the core. This happens if they assume low reaction rates.

Clarkson & Herwig (2020) studied the interaction between convective H shell and He core in massive stars. They found that H shell and He core interact in models adopting the Schwarzschild criterion, while they do not if the Ledoux criterion is assumed. Models with shell interaction can produce up to $1000\times$ more ^{14}N in the shell with respect to models that do not have a shell interaction.

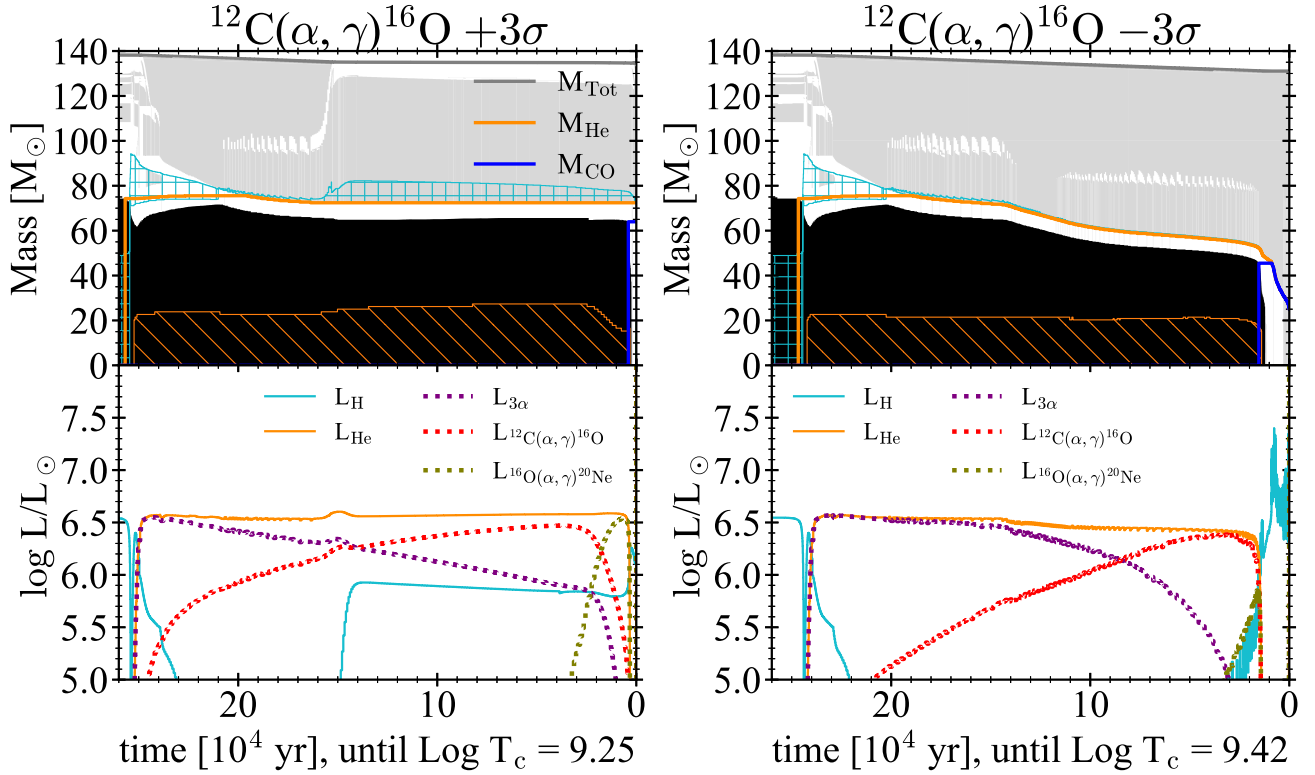


Figure 12. Left-hand panels: Same as Fig. 9, but the evolution is zoomed on the CHeB phase of the $M_{\text{ZAMS}} = 140 M_{\odot}$ star computed with the $^{12}\text{C}(\alpha, \gamma)^{16}\text{O}$ reaction rate $+3\sigma$. Time until the final collapse is in linear scale. In the lower panel, the dotted lines show the contribution to the He luminosity from the CHeB phase main reactions, the triple- α , the $^{12}\text{C}(\alpha, \gamma)^{16}\text{O}$, and the $^{16}\text{O}(\alpha, \gamma)^{20}\text{Ne}$ in purple, red, and green, respectively. Right-hand panels: Same plots as those shown in the left-hand panels, but for a model with $M_{\text{ZAMS}} = 140 M_{\odot}$ and -3σ .

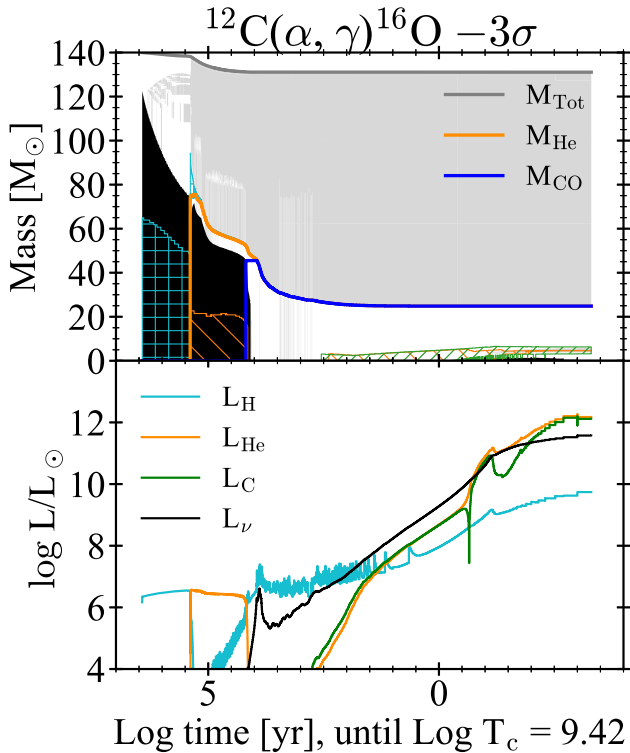


Figure 13. Same as Fig. 9, but for the $M_{\text{ZAMS}} = 140 M_{\odot}$ star with -3σ .

Kaiser et al. (2020) studied the role of overshooting and semi-convection in stars with masses between 15 and $25 M_{\odot}$, adopting different criteria for convection. They found relative uncertainties up to about 70 per cent on the core masses and lifetimes depending on the mixing assumption. Moreover, the relative importance of semi-convection decreases with an increasing amount of overshooting. The amount of overshooting is the main source of uncertainty in all phases.

Recently, Farrell et al. (2020) discuss the role of the H-shell–He-core interaction in metal-poor massive stars. They find that uncertainties related to convective mixing, mass-loss, H–He interactions, and PPI may increase the M_{gap} up to $\approx 85 M_{\odot}$.

In our case, the dredge-up is driven by envelope undershooting. If we turn-off the undershooting, by assuming a $\Lambda_{\text{env}} = 0$ H_p, the dredge-up disappears and all models with $M_{\text{ZAMS}} = 140 M_{\odot}$ become globally unstable and undergo PI (as shown in Fig. 15). The fact that other authors (e.g. Woosley 2017; Takahashi 2018; Marchant et al. 2019; Farmer et al. 2020) do not observe such process in their models is due to different assumptions in the treatment of convection. For instance, stars evolved adopting the Schwarzschild criterion and without semi-convection tend to develop bigger convective regions with respect to stars computed with the Ledoux criterion, due to molecular weight gradient.

4.5 BH mass spectrum

The left-hand panel of Fig. 15 shows the BH mass as a function of M_{ZAMS} and for different $^{12}\text{C}(\alpha, \gamma)^{16}\text{O}$ reaction rates. Since

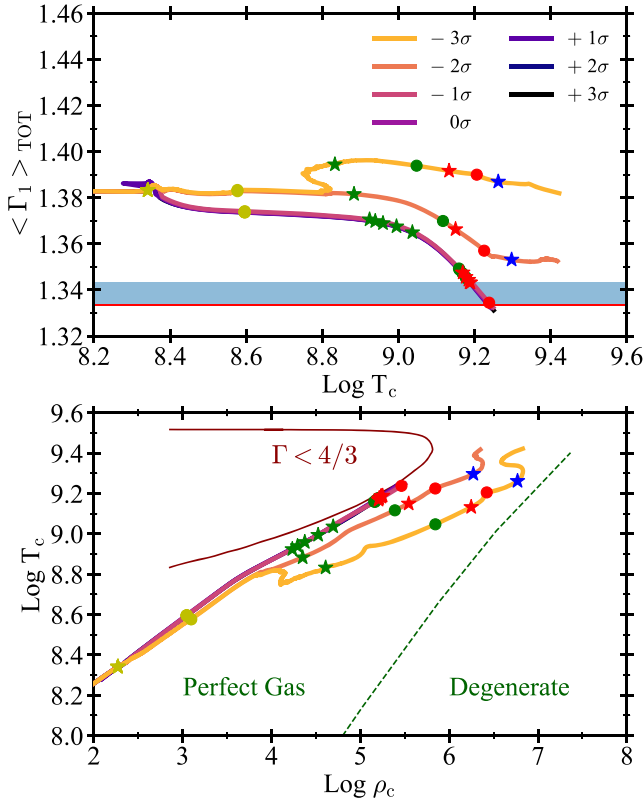


Figure 14. Upper panel: $\langle \Gamma_1 \rangle$ values versus the central temperature of stars with $M_{\text{ZAMS}} = 140 M_{\odot}$. Lower panel: Central density and temperature evolution of models with an initial mass of $140 M_{\odot}$. In both the upper and the lower right-hand panels, we use the same colour code for lines and symbols as in Figs 5 and 10.

we do not know what fraction of the hydrogen envelope is lost during the final collapse, we give a pessimistic and an optimistic estimate for the BH mass in Fig. 15, which bracket this uncertainty. In the pessimistic case (dotted line), the mass of the BH is the same as the final He core mass, which corresponds to assuming that the H envelope is completely lost during the collapse. In the optimistic case (solid line), the mass of the BH is the same as the entire final mass of the star, including all the residual H envelope.

For stars computed with f_{CO} corresponding to $+3\sigma$, $+2\sigma$, and $+1\sigma$, we find a maximum BH mass $M_{\text{BH}} = 60 M_{\odot}$. For stars computed with 0σ , we find a maximum BH mass of $68 M_{\odot}$.

The PI mass gap for models computed with -1σ is between ≈ 80 and $\approx 150 M_{\odot}$. In fact, the dredge-up allows stars with ZAMS mass $M_{\text{ZAMS}} = 160 M_{\odot}$ to leave BHs with mass $\approx 150 M_{\odot}$.

The effect of dredge-up becomes stronger if we consider lower rates for the $^{12}\text{C}(\alpha, \gamma)^{16}\text{O}$ reaction. In the -2σ case, the PI mass gap is between $M_{\text{BH}} = 92 M_{\odot}$ and $110 M_{\odot}$. Finally, models computed with -3σ do not show any mass gap. The mass gap is completely removed by the effect of dredge-up.

The right-hand panel of Fig. 15 shows the same plot of the estimated BH mass but for stars evolved without envelope undershooting ($\Lambda_{\text{env}} = 0 H_{\text{p}}$). In this case, stars more massive than $110 M_{\odot}$ do not undergo the dredge-up during the CHeB phase. Without the dredge-up, the mass gap re-appears, even for low $^{12}\text{C}(\alpha, \gamma)^{16}\text{O}$ rates. The maximum stellar mass that ignites oxygen non-explosively is about $112 M_{\odot}$, in the case with rate -3σ . Hence, if undershooting is

suppressed, the lower edge of the mass gap M_{gap} is at $60 M_{\odot}$ for rates $+3$, $+2$, and $+1$, while $M_{\text{gap}} \approx 68, 80, 92$, and $112 M_{\odot}$ for rates 0 , -1 , -2 , and -3σ , respectively.

Table 3 lists the results obtained for the lower edge of the mass gap for stars with H-rich envelopes, computed with and without envelope undershooting and adopting the optimistic case.

5 DISCUSSION

The recent detection of GW190521 (Abbott et al. 2020b,e), with a primary BH mass of $85^{+21}_{-14} M_{\odot}$ and a secondary BH mass of $66^{+17}_{-18} M_{\odot}$ (90 per cent credible intervals), challenges current models of BH formation.

Here, we have shown that the lower edge of the PI mass gap, M_{gap} , can be as high as $\approx 70 M_{\odot}$, if we assume that the H envelope collapses to a BH directly (Fig. 15). Moreover, if we not only assume that the H envelope collapses but we also take into account the uncertainty on the $^{12}\text{C}(\alpha, \gamma)^{16}\text{O}$ nuclear reaction rate, M_{gap} can be even higher. For the standard $^{12}\text{C}(\alpha, \gamma)^{16}\text{O}$ rate -1σ , the lower edge and the upper edge of the mass gap are ≈ 80 and $\approx 150 M_{\odot}$, respectively. For the standard $^{12}\text{C}(\alpha, \gamma)^{16}\text{O}$ rate -2σ , the lower edge and the upper edge of the mass gap are ≈ 92 and $\approx 110 M_{\odot}$, respectively. Finally for the standard $^{12}\text{C}(\alpha, \gamma)^{16}\text{O}$ rate -3σ , the PI mass gap completely disappears, because of the envelope undershooting effect we just discussed.

The main reasons why previous work has neglected the effect of the H envelope, calculating only models of pure-He stars, is that the H envelope is usually lost during the evolution of an interacting binary star, because of Roche lobe mass transfer and common-envelope episodes. Only metal-poor single stars, or metal-poor stars in loose binary systems (with initial semi-major axis $\gtrsim 10^3 R_{\odot}$, see e.g. Fig. 9 of Spera et al. 2019) can preserve most of their H envelope to the very end of their life.

Loose binary systems cannot lead to BBH mergers via isolated binary evolution, because the initial orbital separation of the BBH is too large to permit coalescence by GW emission. Hence, even in our most optimistic case, it is hard to form systems like GW190521 through isolated binary evolution.

However, in a dense stellar system, the evolution of a single BH (formed from the collapse of a single massive star) and that of a loose BBH (formed from the evolution of a loose binary star) can be very different from that of isolated binary systems (e.g. Sigurdsson & Phinney 1995; Portegies Zwart & McMillan 2000; Banerjee, Baumgardt & Kroupa 2010; Downing et al. 2010; Tanikawa 2013; Samsing, MacLeod & Ramirez-Ruiz 2014; Ziosi et al. 2014; Morscher et al. 2015; Mapelli 2016; Rodriguez, Chatterjee & Rasio 2016; Banerjee 2017, 2020; Samsing 2018; Fragione & Kocsis 2018; Arca Sedda, Askar & Giersz 2018; Kumamoto, Fujii & Tanikawa 2019, 2020; Di Carlo et al. 2019, 2020a, b; Fragione, Loeb & Rasio 2020; Rizzuto et al. 2020). The single BH can pair up with another BH via three-body encounters and dynamical exchanges. A loose BBH can harden (i.e. its semi-major axis shrinks) via three body encounters, speeding up its merger by gravitational waves. The more massive a BH is, the more it is effective in acquiring companions via exchanges and in undergoing dynamical hardening (Heggie 1975; Hills 1976; Hills & Fullerton 1980). For this reason, dynamics favours the formation and merger of the most massive BBHs. Thus, the formation of a BH with mass $85 M_{\odot}$ from the collapse of a single star can easily lead to a system like GW190521 in a dense stellar system. In particular, Di Carlo et al. (2020b) have already shown that the dynamical formation of a merging BBH with masses similar to

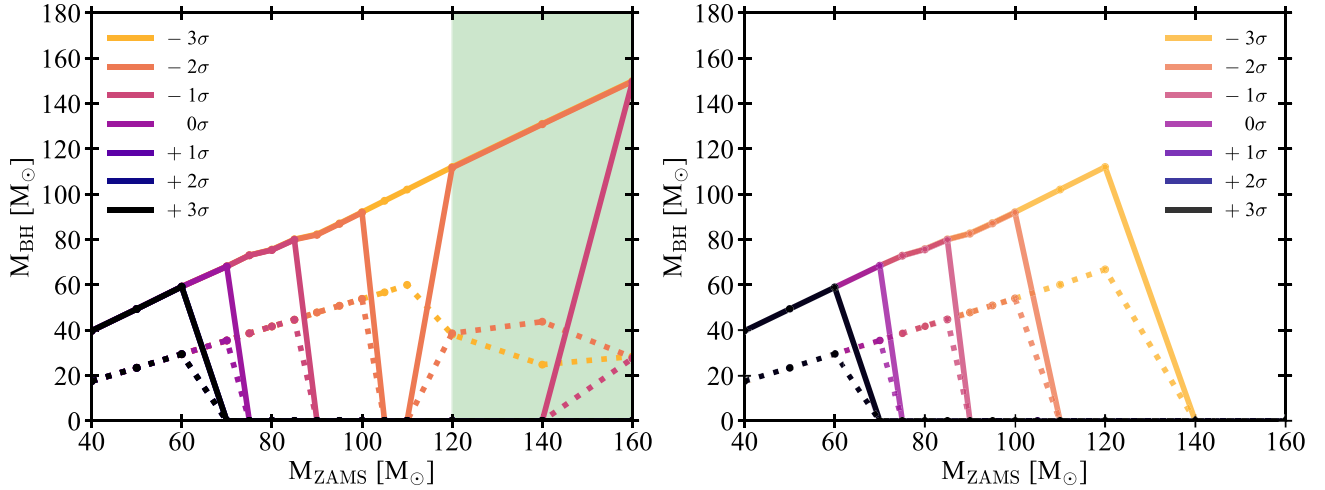


Figure 15. Left-hand panel: Estimated mass of the BH (M_{BH}) as a function of the ZAMS mass of the progenitor star. Different colours indicate stars computed with varying $^{12}\text{C}(\alpha, \gamma)^{16}\text{O}$ reaction rates. Solid lines indicate the total final mass of the star. Dotted lines indicate the final He core mass. As discussed in the text, the actual M_{BH} mass will be between the He core mass (pessimistic case, dotted lines) and the total final mass of the star (optimistic case, solid lines). The green area indicates models that experience dredge-up during the CHeB. Right-hand panel: Same as the left-hand panel but for a set of tracks computed without envelope undershooting.

Table 3. Lower edge of the PI mass gap (M_{gap}) from stars with H-rich envelopes.

Rate	$\Lambda_{\text{env}} = 0.7 \text{ Hp}$	$\Lambda_{\text{env}} = 0 \text{ Hp}$
	M_{gap} [M_{\odot}]	M_{gap} [M_{\odot}]
-3σ	None	112
-2σ	92	92
-1σ	80	80
0σ	68	68
$+1\sigma$	60	60
$+2\sigma$	60	60
$+3\sigma$	60	60

Note. Column 1: rate assumed for the $^{12}\text{C}(\alpha, \gamma)^{16}\text{O}$ reaction; column 2: lower edge of the mass gap M_{gap} for models computed with envelope undershooting; column 3: M_{gap} for models computed without envelope undershooting. ‘None’ indicates that no star undergoes PI.

GW190521 (88 and 48 M_{\odot}) is possible in a young dense star cluster.

Moreover, a $\approx 85 M_{\odot}$ BH born from the direct collapse of a star will preserve most (if not all) the spin of its progenitor star, leading to a fast rotating BH (Mapelli et al. 2020). If this BH acquires a companion via dynamical interactions, the spins of the primary and of the secondary BH will be isotropically oriented, possibly leading to a large precession spin (χ_p). This feature is consistent with the properties of GW190521 (Abbott et al. 2020b,e).

Recently, Belczynski (2020) even suggested that isolated binary star evolution at low metallicity can produce BBHs with masses consistent with GW190521, when the uncertainties on the $^{12}\text{C}(\alpha, \gamma)^{16}\text{O}$ rate are taken into account (assuming -2.5σ rates from Farmer et al. 2020) and when extreme stellar masses ($M_{\text{ZAMS}} \approx 180 M_{\odot}$) are considered. However, the isolated binary evolution channel predicts a lower χ_p than the one estimated by Abbott et al. (2020e) within the 90 per cent credible interval.

6 CONCLUSIONS

We investigated the lower edge of the pair-instability (PI) BH mass gap (M_{gap}), by means of the PARSEC evolutionary code.

We evolved (i) a set of pure-He stars with initial masses between 20 and 100 M_{\odot} and with metallicity $Z = 0.001$, (ii) a set of stars with H envelopes, with masses ranging from 40 to 160 M_{\odot} and with $Z = 0.0003$. For both sets, we have varied the $^{12}\text{C}(\alpha, \gamma)^{16}\text{O}$ rates from -3σ to $+3\sigma$, where 1σ is the given confidence error by the STARLIB library. We have followed the evolution of the models until oxygen burning, if the star remains globally stable. We find that, changing the $^{12}\text{C}(\alpha, \gamma)^{16}\text{O}$ rates directly affects the carbon-to-oxygen ratio at the end of the CHeB.

In the case of pure-He stars, the lower edge of the mass gap (M_{gap}) varies from 68 M_{\odot} (-3σ $^{12}\text{C}(\alpha, \gamma)^{16}\text{O}$ rate) to 20 M_{\odot} ($+3\sigma$ rate). For the standard $^{12}\text{C}(\alpha, \gamma)^{16}\text{O}$ rate, we find $M_{\text{gap}} \approx 30 M_{\odot}$.

Since we use a hydro-static code, we do not follow the evolution through the PPI phase. We conservatively assume that both stars going through PPI and stars going through PISN leave no compact objects. Since stars going through PPI might be able to stabilize and form BHs by direct collapse (Marchant et al. 2019), our findings are robust lower limits for the lower edge of the mass gap. For this reason, we find lower values of M_{gap} with respect to previous works (Woosley 2017; Leung et al. 2019; Farmer et al. 2020) in case of pure-He stars.

In the case of stellar models with an hydrogen envelope, the main uncertainty on the final BH mass is represented by the fate of the envelope (Mapelli et al. 2020). Here, we consider a pessimistic estimate in which only the He core collapses to the final BH and an optimistic approach in which the H envelope entirely collapses to the final BH.

Adopting the standard $^{12}\text{C}(\alpha, \gamma)^{16}\text{O}$ rate and assuming an optimistic approach, we find $M_{\text{gap}} = 68 M_{\odot}$. Assuming the $+3\sigma$ $^{12}\text{C}(\alpha, \gamma)^{16}\text{O}$ rate, this value lowers to $M_{\text{gap}} = 59 M_{\odot}$.

If we consider lower values than the standard $^{12}\text{C}(\alpha, \gamma)^{16}\text{O}$ rate, we find that the interaction between the hydrogen envelope and the He core may result in a very different evolution of the star. Models computed with low $^{12}\text{C}(\alpha, \gamma)^{16}\text{O}$ rates ($-1, -2, -3\sigma$) and with an

initial mass higher than $110 M_{\odot}$ may experience an important dredge-up during the CHEB that extracts matter from the core enriching the envelope.

Stars experiencing such dredge-up are more stable and ignite oxygen in a non-explosive way, despite their high mass. The most remarkable result is that the PI mass gap narrows in the -1 and -2σ cases, and it completely disappears in the -3σ case.

In the -3σ case, all our models evolve until the core collapse, without undergoing PI. In case of -2σ and -1σ we find a mass gap between $92\text{--}110 M_{\odot}$ and $80\text{--}150 M_{\odot}$, respectively.

For higher rates ($0, +1, +2, +3 \sigma$), the dredge-up does not happen and the lower edge of the mass gap is $M_{\text{gap}} \approx 60\text{--}70 M_{\odot}$ in the optimistic case ($M_{\text{gap}} \approx 30\text{--}40 M_{\odot}$ in the pessimistic case).

We confirm that the $^{12}\text{C}(\alpha, \gamma)^{16}\text{O}$ reaction has a strong impact on the final fate of a massive star, as found by other authors (Takahashi 2018; Farmer et al. 2019, 2020). In addition, we show that another challenging phenomenon could be the occurrence of an efficient dredge-up at the bottom of the H-rich envelope, in the advanced phases. Stars that experience such a dredge-up may develop envelopes heavily enriched by N and O. In the case such enriched envelopes are ejected, their contribution to stellar yields, especially N, may be significant. This could be relevant for the chemical evolution of nitrogen at low metallicity (Pettini et al. 2008; Vincenzo et al. 2016).

Taking into account the uncertainties on the collapse of the H envelope and on the $^{12}\text{C}(\alpha, \gamma)^{16}\text{O}$ reaction rate, we can explain the formation of massive BHs such as the primary component of GW190521 (Abbott et al. 2020b,e) with the collapse of a single massive metal-poor star. If such massive BH forms in a dense stellar cluster, it might have a chance to dynamically pair up with another massive BH, leading to the formation of a GW190521-like system, with a large precession spin.

ACKNOWLEDGEMENTS

We are grateful to the anonymous referee for their useful comments. We thank Rob Farmer for the fruitful discussions and for providing us MESA pure-He models. MM, GC, and GI acknowledge financial support from the European Research Council for the ERC Consolidator grant DEMOBLACK, under contract no. 770017. AB acknowledges support from PRIN-MIUR 2017 prot. 20173ML3WW. This research made use of NUMPY (Harris et al. 2020), SCIPY (Virtanen et al. 2020), IPYTHON (Perez & Granger 2007). For the plots, we used MATPLOTLIB, a Python library for publication of quality graphics (Hunter 2007).

DATA AVAILABILITY

The data underlying this article will be shared on reasonable request to the corresponding author.

REFERENCES

Abbott B. P. et al., 2016a, *Phys. Rev. X*, 6, 041015
 Abbott B. P. et al., 2016b, *Phys. Rev. Lett.*, 116, 061102
 Abbott B. P. et al., 2016c, *ApJ*, 818, L22
 Abbott B. P. et al., 2017, *Phys. Rev. Lett.*, 119, 161101
 Abbott B. P. et al., 2019a, *Phys. Rev. X*, 9, 031040
 Abbott B. P. et al., 2019b, *ApJ*, 882, L24
 Abbott R. et al., 2020a, *Phys. Rev. D*, 102, 043015
 Abbott R. et al., 2020b, *Phys. Rev. Lett.*, 125, 101102
 Abbott B. P. et al., 2020c, *ApJ*, 892, L3

Abbott R. et al., 2020d, *ApJ*, 896, L44
 Abbott R. et al., 2020e, *ApJ*, 900, L13
 Alongi M., Bertelli G., Bressan A., Chiosi C., 1991, *A&A*, 244, 95
 Arca Sedda M., Askar A., Giersz M., 2018, *MNRAS*, 479, 4652
 Arcavi I. et al., 2017, *Nature*, 551, 210
 Banerjee S., 2017, *MNRAS*, 467, 524
 Banerjee S., , 2020, *MNRAS*, 500, 3002
 Banerjee S., Baumgardt H., Kroupa P., 2010, *MNRAS*, 402, 371
 Belczynski K. et al., 2016, *A&A*, 594, A97
 Belczynski K., 2020, *ApJ Lett.*, 905, L15,
 Böhm-Vitense E., 1958, *ZAp*, 46, 108
 Bertelli G., Bressan A. G., Chiosi C., 1985, *A&A*, 150, 33
 Bestenlehner J. M. et al., 2014, *A&A*, 570, A38
 Bressan A., Marigo P., Girardi L., Salasnich B., Dal Cero C., Rubele S., Nanni A., 2012, *MNRAS*, 427, 127
 Brunish W. M., Becker S. A., 1990, *ApJ*, 351, 258
 Buchmann L., 1996, *ApJ*, 468, L127
 Caffau E., Ludwig H. G., Steffen M., Freytag B., Bonifacio P., 2011, *Sol. Phys.*, 268, 255
 Caughlan G. R., Fowler W. A., 1988, *At. Data Nucl. Data Tables*, 40, 283
 Chatzopoulos E., Wheeler J. C., 2012, *ApJ*, 748, 42
 Chatzopoulos E., Wheeler J. C., Couch S. M., 2013, *ApJ*, 776, 129
 Chen Y., Bressan A., Girardi L., Marigo P., Kong X., Lanza A., 2015, *MNRAS*, 452, 1068
 Chen K.-J., Woosley S., Heger A., Almgren A., Whalen D. J., 2014, *ApJ*, 792, 28
 Clarkson O., Herwig F., 2020, *MNRAS*, 500, 2685
 Costa G., Girardi L., Bressan A., Marigo P., Rodrigues T. S., Chen Y., Lanza A., Goudfrooij P., 2019, *MNRAS*, 485, 4641
 Cyburt R. H. et al., 2010, *ApJS*, 189, 240
 Cyburt R. H., Hoffman R., Woosley S., 2012, Re-evaluation of Buchmann 1996 C12(a,g) and Hoffman Ca40(a,g) and Ti44(a,p) rates, REACLIB, <https://reaclib.jinaweb.org/labels.php?action=viewLabel&label=chw0>
 deBoer R. J. et al., 2017, *Rev. Mod. Phys.*, 89, 035007
 Di Carlo U. N. et al., 2020b, *MNRAS*, 498, 495
 Di Carlo U. N., Giacobbo N., Mapelli M., Pasquato M., Spera M., Wang L., Haardt F., 2019, *MNRAS*, 487, 2947
 Di Carlo U. N., Mapelli M., Bouffanais Y., Giacobbo N., Santoliquido F., Bressan A. r., Spera M., Haardt F., 2020a, *MNRAS*, 497, 1043
 Downing J. M. B., Benacquista M. J., Giersz M., Spurzem R., 2010, *MNRAS*, 407, 1946
 Farmer R., Renzo M., de Mink S. E., Marchant P., Justham S., 2019, *ApJ*, 887, 53
 Farmer R., Renzo M., de Mink S., Fishbach M., Justham S., 2020, *ApJ Lett.*, 902, L36
 Farrell E. J., Groh J. H., Hirschi R., Murphy L., Kaiser E., Ekström S., Georgy C., Meynet G., 2020, *ApJ Lett.*, 902, L36
 Fields C. E., Timmes F. X., Farmer R., Petermann I., Wolf W. M., Couch S. M., 2018, *ApJS*, 234, 19
 Fragione G., Kocsis B., 2018, *Phys. Rev. Lett.*, 121, 161103
 Fragione G., Loeb A., Rasio F. A., 2020, *ApJ*, 902, L26
 Fu X., Bressan A., Marigo P., Girardi L., Montalbán J., Chen Y., Nanni A., 2018, *MNRAS*, 476, 496
 Giacobbo N., Mapelli M., Spera M., 2018, *MNRAS*, 474, 2959
 Gomez S. et al., 2019, *ApJ*, 881, 87
 Gräfener G., Hamann W. R., 2008, *A&A*, 482, 945
 Haemmerlé L., Meynet G., 2019, *A&A*, 623, L7
 Haft M., Raffelt G., Weiss A., 1994, *ApJ*, 425, 222
 Harris C. R. et al., 2020, *Nature*, 585, 357
 Heger A., Woosley S. E., 2002, *ApJ*, 567, 532
 Heggie D. C., 1975, *MNRAS*, 173, 729
 Hills J. G., 1976, *MNRAS*, 175, 1P
 Hills J. G., Fullerton L. W., 1980, *AJ*, 85, 1281
 Humphreys R. M., Davidson K., 1984, *Science*, 223, 243
 Hunter J. D., 2007, *Comput. Sci. Eng.*, 9, 90
 Iben Icko J., 1967, *ARA&A*, 5, 571
 Iben I. J., 1974, *ARA&A*, 12, 215

- Iglesias C. A., Rogers F. J., 1996, *ApJ*, 464, 943
- Itoh N., Kohyama Y., 1983, *ApJ*, 275, 858
- Itoh N., Uchida S., Sakamoto Y., Kohyama Y., Nozawa S., 2008, *ApJ*, 677, 495
- Jiang Y.-F., Cantiello M., Bildsten L., Quataert E., Blaes O., Stone J., 2018, *Nature*, 561, 498
- Kaiser E. A., Hirschi R., Arnett W. D., Georgy C., Scott L. J. A., Cristini A., 2020, *MNRAS*, 496, 1967
- Keszthelyi Z. et al., 2020, *MNRAS*, 493, 518
- Kippenhahn R., Weigert A., Weiss A., 2012, *Stellar Structure and Evolution*. Springer-Verlag, Berlin
- Kumamoto J., Fujii M. S., Tanikawa A., 2019, *MNRAS*, 486, 3942
- Kumamoto J., Fujii M. S., Tanikawa A., 2020, *MNRAS*, 495, 4268
- Kunz R., Fey M., Jaeger M., Mayer A., Hammer J. W., Staudt G., Harissopulos S., Paradellis T., 2002, *ApJ*, 567, 643
- Ledoux P., Walraven T., 1958, *Handbuch der Physik*, 51, 353
- Leung S.-C., Nomoto K., Blinnikov S., 2019, *ApJ*, 887, 72
- Limongi M., Chieffi A., 2018, *ApJS*, 237, 13
- Mapelli M., 2016, *MNRAS*, 459, 3432
- Mapelli M., Giacobbo N., Santoliquido F., Artale M. C., 2019, *MNRAS*, 487, 2
- Mapelli M., Spera M., Montanari E., Limongi M., Chieffi A., Giacobbo N., Bressan A., Bouffanais Y., 2020, *ApJ*, 888, 76
- Marchant P., Moriya T., 2020, *A&A*, 640, L18
- Marchant P., Renzo M., Farmer R., Pappas K. M. W., Taam R. E., de Mink S. E., Kalogera V., 2019, *ApJ*, 882, 36
- Marigo P., Aringer B., 2009, *A&A*, 508, 1539
- Marigo P., Bressan A., Nanni A., Girardi L., Pumo M. L., 2013, *MNRAS*, 434, 488
- Morscher M., Pattabiraman B., Rodriguez C., Rasio F. A., Umbreit S., 2015, *ApJ*, 800, 9
- Munakata H., Kohyama Y., Itoh N., 1985, *ApJ*, 296, 197
- Paxton B. et al., 2013, *ApJS*, 208, 4
- Paxton B. et al., 2015, *ApJS*, 220, 15
- Paxton B. et al., 2018, *ApJS*, 234, 34
- Paxton B., Bildsten L., Dotter A., Herwig F., Lesaffre P., Timmes F., 2011, *ApJS*, 192, 3
- Perez F., Granger B. E., 2007, *Comput. Sci. Engin.*, 9, 21
- Pettini M., Zych B. J., Steidel C. C., Chaffee F. H., 2008, *MNRAS*, 385, 2011
- Portegies Zwart S. F., McMillan S. L. W., 2000, *ApJ*, 528, L17
- Rapagnani D. et al., 2017, *Nucl. Instrum. Methods Phys. Res. B*, 407, 217
- Renzo M., Farmer R. J., Justham S., de Mink S. E., Göteborg Y., Marchant P., 2020, *MNRAS*, 493, 4333
- Rizzuto F. P. et al., 2020, *MNRAS*
- Rodriguez C. L., Chatterjee S., Rasio F. A., 2016, *Phys. Rev. D*, 93, 084029
- Sallaska A. L., Iliadis C., Champagne A. E., Goriely S., Starrfield S., Timmes F. X., 2013, *ApJS*, 207, 18
- Samsing J., 2018, *Phys. Rev. D*, 97, 103014
- Samsing J., MacLeod M., Ramirez-Ruiz E., 2014, *ApJ*, 784, 71
- Sander A. A. C., Hamann W. R., Todt H., Hainich R., Shenar T., Ramachandran V., Osinkova L. M., 2019, *A&A*, 621, A92
- Sigurdsson S., Phinney E. S., 1995, *ApJS*, 99, 609
- Song H., Meynet G., Li Z., Peng W., Zhang R., Zhan Q., 2020, *ApJ*, 892, 41
- Spera M., Mapelli M., 2017, *MNRAS*, 470, 4739
- Spera M., Mapelli M., Giacobbo N., Trani A. A., Bressan A., Costa G., 2019, *MNRAS*, 485, 889
- Stevenson S., Sampson M., Powell J., Vigna-Gómez A., Neijssel C. J., Szécsi D., Mandel I., 2019, *ApJ*, 882, 121
- Stothers R. B., 1999, *MNRAS*, 305, 365
- Sukhbold T., Adams S., 2020, *MNRAS*, 492, 2578
- Sukhbold T., Ertl T., Woosley S. E., Brown J. M., Janka H. T., 2016, *ApJ*, 821, 38
- Takahashi K., 2018, *ApJ*, 863, 153
- Tang J., Bressan A., Rosenfield P., Slemmer A., Marigo P., Girardi L., Bianchi L., 2014, *MNRAS*, 445, 4287
- Tanikawa A., 2013, *MNRAS*, 435, 1358
- Tanikawa A., Susa H., Yoshida T., Trani A. A., Kinugawa T., 2020a, preprint([arXiv:2008.01890](https://arxiv.org/abs/2008.01890))
- Tanikawa A., Kinugawa T., Yoshida T., Hijikawa K., Umeda H., 2020b, preprint([arXiv:2010.07616](https://arxiv.org/abs/2010.07616))
- Timmes F. X., Arnett D., 1999, *ApJS*, 125, 277
- Tur C., Heger A., Austin S. M., 2007, *ApJ*, 671, 821
- Tur C., Heger A., Austin S. M., 2010, *ApJ*, 718, 357
- van Son L. A. C. et al., 2020, *ApJ*, 897, 100
- Vincenzo F., Belfiore F., Maiolino R., Matteucci F., Ventura P., 2016, *MNRAS*, 458, 3466
- Vink J. S., 2011, *Ap&SS*, 336, 163
- Vink J. S., 2015, in Hamann W.-R., Sander A., Todt H., eds, *Wolf-Rayet Stars*. p. 133
- Vink J. S., de Koter A., Lamers H. J. G. L. M., 2000, *A&A*, 362, 295
- Vink J. S., de Koter A., Lamers H. J. G. L. M., 2001, *A&A*, 369, 574
- Virtanen P. et al., 2020, *Nat. Methods*, 17, 261
- Weaver T. A., Woosley S. E., 1993, *Phys. Rep.*, 227, 65
- Woosley S. E., 2017, *ApJ*, 836, 244
- Woosley S. E., 2019, *ApJ*, 878, 49
- Woosley S. E., Heger A., 2007, *Phys. Rep.*, 442, 269
- Woosley S. E., Blinnikov S., Heger A., 2007, *Nature*, 450, 390
- Ziosi B. M., Mapelli M., Branchesi M., Tormen G., 2014, *MNRAS*, 441, 3703

APPENDIX A: TABLES

Tables A1 and A2 show the results obtained for pure-He and full stars. More details in Sections 3.2 and 4.2.

Table A1. Pure He stars' results. See text for details.

$M_{\text{He-ZAMS}}$ [M_{\odot}]	Rate	M_{He} [M_{\odot}]	M_{CO} [M_{\odot}]	$X_{\text{C-He}}$ Mass frac.	$X_{\text{O-C-He}}$ Mass frac.	M_{Pre} [M_{\odot}]	Log T_{c} [K]	$X_{\text{O-C-Pre}}$ Mass frac.	$\langle \Gamma_1 \rangle_{\text{TOT}}$	Fate
20	-3σ	19.31	15.36	0.49	0.49	19.30	9.378	0.046	0.0553	CC
20	-2σ	19.29	15.34	0.41	0.58	19.28	9.405	0.013	0.0534	CC
20	-1σ	19.27	15.28	0.33	0.66	19.26	9.419	0.013	0.0476	CC
20	0σ	19.24	15.28	0.24	0.75	19.23	9.401	0.110	0.0393	CC
20	$+1\sigma$	19.22	15.29	0.15	0.84	19.21	9.415	0.175	0.0256	CC
20	$+2\sigma$	19.19	15.33	0.07	0.91	19.19	9.419	0.224	0.0187	CC
20	$+3\sigma$	19.18	15.41	0.01	0.94	19.17	9.421	0.234	0.0175	CC
30	-3σ	29.07	24.34	0.46	0.52	29.09	9.404	0.075	0.0389	CC
30	-2σ	29.04	24.29	0.37	0.61	29.06	9.409	0.094	0.0339	CC
30	-1σ	29.01	24.30	0.29	0.70	29.03	9.402	0.129	0.0249	CC
30	0σ	28.98	24.27	0.19	0.79	28.99	9.417	0.218	0.0096	CC
30	$+1\sigma$	28.94	24.28	0.11	0.87	28.96	9.418	0.313	0.0021	CC
30	$+2\sigma$	28.92	24.31	0.04	0.92	28.93	9.417	0.405	-0.0015	PI
30	$+3\sigma$	28.90	24.33	0.01	0.91	28.92	9.418	0.387	-0.0019	PI
40	-3σ	38.87	33.23	0.43	0.54	38.89	9.415	0.092	0.0259	CC
40	-2σ	38.83	33.21	0.34	0.63	38.86	9.414	0.136	0.0185	CC
40	-1σ	38.79	33.22	0.26	0.72	38.82	9.410	0.210	0.0094	CC
40	0σ	38.76	33.20	0.17	0.81	38.78	9.429	0.270	-0.0068	PI
40	$+1\sigma$	38.73	33.22	0.09	0.88	38.75	9.326	0.906	-0.0026	PI
40	$+2\sigma$	38.69	33.18	0.03	0.91	38.72	9.350	0.923	-0.0063	PI
40	$+3\sigma$	38.67	33.19	0.00	0.89	38.70	9.397	0.698	-0.0098	PI
50	-3σ	48.68	42.16	0.41	0.56	48.72	9.404	0.098	0.0305	CC
50	-2σ	48.64	42.16	0.32	0.65	48.68	9.396	0.126	0.0247	CC
50	-1σ	48.60	42.08	0.23	0.73	48.63	9.411	0.306	-0.0047	PI
50	0σ	48.56	42.12	0.15	0.82	48.59	9.379	0.719	-0.0108	PI
50	$+1\sigma$	48.51	42.12	0.07	0.88	48.55	9.294	0.915	-0.0069	PI
50	$+2\sigma$	48.48	42.11	0.02	0.90	48.52	9.269	0.933	-0.0030	PI
50	$+3\sigma$	48.46	42.04	0.00	0.87	48.49	9.284	0.916	-0.0057	PI
55	-3σ	53.60	46.68	0.40	0.56	53.64	9.406	0.107	0.0276	CC
55	-2σ	53.55	46.56	0.31	0.65	53.59	9.414	0.138	0.0202	CC
55	-1σ	53.51	46.62	0.22	0.74	53.55	9.397	0.617	-0.0088	PI
55	0σ	53.46	46.57	0.14	0.82	53.50	9.287	0.870	-0.0090	PI
55	$+1\sigma$	53.42	46.53	0.06	0.88	53.46	9.276	0.916	-0.0077	PI
55	$+2\sigma$	53.39	46.57	0.02	0.89	53.42	9.244	0.917	-0.0019	PI
55	$+3\sigma$	53.36	46.53	0.00	0.86	53.40	9.265	0.909	-0.0059	PI
60	-3σ	58.51	51.20	0.39	0.57	58.56	9.399	0.102	0.0237	CC
60	-2σ	58.47	51.08	0.30	0.66	58.51	9.381	0.147	0.0162	CC
60	-1σ	58.43	51.06	0.22	0.74	58.46	9.358	0.707	-0.0108	PI
60	0σ	58.37	51.04	0.13	0.82	58.41	9.272	0.872	-0.0098	PI
60	$+1\sigma$	58.33	51.02	0.06	0.88	58.37	9.266	0.914	-0.0093	PI
60	$+2\sigma$	58.29	51.03	0.02	0.88	58.33	9.250	0.914	-0.0063	PI
60	$+3\sigma$	58.27	51.08	0.00	0.85	58.31	9.263	0.901	-0.0089	PI
65	-3σ	63.44	55.61	0.38	0.57	63.48	9.409	0.126	0.0215	CC
65	-2σ	63.38	55.64	0.30	0.66	63.43	9.381	0.166	0.0142	CC
65	-1σ	63.33	55.63	0.21	0.75	63.38	9.275	0.815	-0.0098	PI
65	0σ	63.29	55.56	0.12	0.82	63.33	9.258	0.873	-0.0102	PI
65	$+1\sigma$	63.24	55.55	0.05	0.87	63.28	9.251	0.905	-0.0093	PI
65	$+2\sigma$	63.20	55.49	0.01	0.88	63.25	9.250	0.907	-0.0091	PI
65	$+3\sigma$	63.18	55.44	0.00	0.85	63.22	9.249	0.885	-0.0090	PI
70	-3σ	68.35	60.15	0.38	0.58	68.41	9.418	0.105	0.0186	CC
70	-2σ	68.30	60.13	0.29	0.67	68.35	9.375	0.653	-0.0099	PI
70	-1σ	68.25	60.15	0.20	0.75	68.30	9.261	0.817	-0.0111	PI
70	0σ	68.20	60.00	0.12	0.83	68.25	9.248	0.869	-0.0110	PI
70	$+1\sigma$	68.16	60.02	0.05	0.87	68.20	9.244	0.896	-0.0104	PI
70	$+2\sigma$	68.12	60.02	0.01	0.87	68.16	9.234	0.885	-0.0085	PI
70	$+3\sigma$	68.09	59.96	0.00	0.84	68.14	9.238	0.865	-0.0094	PI
80	-3σ	78.21	69.19	0.37	0.58	78.26	9.316	0.681	-0.0076	PI
80	-2σ	78.15	69.17	0.28	0.67	78.21	9.247	0.759	-0.0095	PI
80	-1σ	78.09	69.16	0.19	0.75	78.15	9.227	0.795	-0.0109	PI

Table A1 – *continued*

M _{He-ZAMS} [M _⊙]	Rate	M _{He} [M _⊙]	M _{CO} [M _⊙]	XC _{c-He} Mass frac.	XO _{c-He} Mass frac.	M _{Pre} [M _⊙]	Log T _c [K]	XO _{c-Pre} Mass frac.	⟨Γ ₁ ⟩ _{TOT}	Fate
80	0 σ	78.02	69.07	0.11	0.83	78.09	9.226	0.836	−0.0113	PI
80	+1 σ	77.98	69.00	0.04	0.87	78.04	9.220	0.863	−0.0102	PI
80	+2 σ	77.94	68.96	0.01	0.86	78.00	9.221	0.863	−0.0105	PI
80	+3 σ	77.91	68.91	0.00	0.83	77.98	9.222	0.837	−0.0107	PI
90	−3 σ	88.06	78.15	0.36	0.59	88.13	9.232	0.695	−0.0087	PI
90	−2 σ	87.99	78.05	0.27	0.68	88.06	9.203	0.666	−0.0095	PI
90	−1 σ	87.94	78.13	0.18	0.76	88.00	9.204	0.737	−0.0103	PI
90	0 σ	87.87	78.05	0.10	0.83	87.94	9.201	0.804	−0.0100	PI
90	+1 σ	87.82	78.00	0.04	0.86	87.89	9.204	0.851	−0.0107	PI
90	+2 σ	87.78	77.97	0.01	0.85	87.85	9.201	0.848	−0.0099	PI
90	+3 σ	87.75	77.96	0.00	0.82	87.82	9.202	0.821	−0.0103	PI
100	−3 σ	97.92	87.20	0.35	0.59	97.99	9.194	0.562	−0.0105	PI
100	−2 σ	97.84	87.10	0.26	0.68	97.92	9.193	0.642	−0.0110	PI
100	−1 σ	97.78	87.08	0.17	0.76	97.86	9.194	0.726	−0.0115	PI
100	0 σ	97.71	87.08	0.09	0.82	97.79	9.192	0.801	−0.0111	PI
100	+1 σ	97.66	87.03	0.04	0.85	97.74	9.190	0.845	−0.0107	PI
100	+2 σ	97.61	87.03	0.01	0.84	97.69	9.188	0.839	−0.0102	PI
100	+3 σ	97.59	86.96	0.00	0.81	97.67	9.190	0.811	−0.0107	PI

Note. Column 1: He-ZAMS mass. Column 2: rate assumed for the $^{12}\text{C}(\alpha, \gamma)^{16}\text{O}$ reaction. Column 3: mass of the helium core at the end of the He-MS. Column 4: mass of the CO core at the end of the He-MS. Columns 5 and 6: carbon and oxygen central mass fractions at the end of the He-MS, respectively. Column 7: final pre-supernova mass (M_{Pre}). Column 8: central temperature of the last model. Column 9: oxygen central mass fraction at the end of the computation. Column 10: $\langle\Gamma_1\rangle_{\text{TOT}}$. Column 11: final fate of the star, which can be either core collapse (CC) or pair-instability (PI).

Table A2. Results for stars with hydrogen envelopes. See text for details.

M _{ZAMS} [M _⊙]	Rate	M _{He} [M _⊙]	M _{CO} [M _⊙]	XC _{c-He} Mass frac.	XO _{c-He} Mass frac.	M _{Pre} [M _⊙]	Log T _c [K]	XO _{c-Pre} Mass frac.	⟨Γ ₁ ⟩ _{Core} –	⟨Γ ₁ ⟩ _{TOT} –	Fate	Dredge-up
40	−3 σ	17.50	13.81	0.50	0.49	39.75	9.365	0.013	0.0617	0.0617	CC	No
40	−2 σ	17.51	13.81	0.42	0.57	39.75	9.185	0.627	0.0603	0.0604	CC	No
40	−1 σ	17.51	13.81	0.34	0.66	39.76	9.409	0.011	0.0544	0.0546	CC	No
40	0 σ	17.51	13.81	0.24	0.75	39.76	9.397	0.087	0.0470	0.0474	CC	No
40	+1 σ	17.52	13.82	0.15	0.84	39.76	9.400	0.257	0.0361	0.0367	CC	No
40	+2 σ	17.52	13.82	0.07	0.91	39.76	9.378	0.522	0.0334	0.0341	CC	No
40	+3 σ	17.53	13.82	0.01	0.94	39.76	9.417	0.205	0.0272	0.0279	CC	No
50	−3 σ	23.42	19.15	0.47	0.51	49.39	9.189	0.582	0.0489	0.0488	CC	No
50	−2 σ	23.42	19.16	0.39	0.60	49.39	9.402	0.070	0.0450	0.0451	CC	No
50	−1 σ	23.42	19.16	0.30	0.68	49.39	9.440	0.000	0.0364	0.0366	CC	No
50	0 σ	23.42	19.16	0.21	0.77	49.38	9.411	0.144	0.0294	0.0297	CC	No
50	+1 σ	23.42	19.16	0.12	0.86	49.37	9.400	0.323	0.0216	0.0220	CC	No
50	+2 σ	23.42	19.16	0.05	0.92	49.36	9.421	0.239	0.0129	0.0134	CC	No
50	+3 σ	23.42	19.17	0.01	0.93	49.35	9.422	0.242	0.0120	0.0126	CC	No
60	−3 σ	29.42	24.63	0.45	0.53	59.24	9.405	0.077	0.0383	0.0384	CC	No
60	−2 σ	29.42	24.64	0.37	0.62	59.24	9.435	0.016	0.0323	0.0326	CC	No
60	−1 σ	29.42	24.62	0.28	0.70	59.24	9.388	0.209	0.0264	0.0268	CC	No
60	0 σ	29.45	24.63	0.19	0.79	59.22	9.416	0.181	0.0162	0.0168	CC	No
60	+1 σ	29.45	24.63	0.10	0.87	59.21	9.422	0.237	0.0057	0.0064	CC	No
60	+2 σ	29.45	24.63	0.04	0.92	59.20	9.421	0.312	0.0018	0.0026	CC	No
60	+3 σ	29.45	24.63	0.01	0.91	59.18	9.419	0.332	0.0016	0.0024	CC	No
70	−3 σ	35.42	30.25	0.43	0.54	68.21	9.441	0.001	0.0278	0.0280	CC	No
70	−2 σ	35.42	30.25	0.35	0.63	68.17	9.438	0.033	0.0229	0.0232	CC	No
70	−1 σ	35.42	30.25	0.26	0.72	68.15	9.417	0.160	0.0151	0.0156	CC	No
70	0 σ	35.42	30.38	0.17	0.80	68.09	9.420	0.243	0.0028	0.0035	CC	No
70	+1 σ	35.42	30.38	0.09	0.88	68.08	9.418	0.351	−0.0037	−0.0030	PI	No
70	+2 σ	35.46	30.37	0.03	0.91	68.07	9.427	0.302	−0.0076	−0.0068	PI	No
70	+3 σ	35.46	30.38	0.00	0.89	68.09	9.414	0.458	−0.0065	−0.0057	PI	No
75	−3 σ	38.58	33.32	0.43	0.55	73.10	9.413	0.103	0.0255	0.0258	CC	No
75	−2 σ	38.58	33.32	0.34	0.64	73.07	9.415	0.130	0.0184	0.0188	CC	No

Table A2 – continued

M _{ZAMS} [M _⊙]	Rate	M _{He} [M _⊙]	M _{CO} [M _⊙]	X _{C-He} Mass frac.	X _{O-He} Mass frac.	M _{Pre} [M _⊙]	Log T _c [K]	X _{O-Pre} Mass frac.	(Γ ₁) _{Core} –	(Γ ₁) _{TOT} –	Fate	Dredge-up
75	−1σ	38.58	33.32	0.25	0.72	73.05	9.394	0.330	0.0116	0.0121	CC	No
75	0σ	38.58	33.32	0.16	0.81	73.03	9.417	0.305	−0.0021	−0.0013	PI	No
75	+1σ	38.58	33.33	0.08	0.88	73.01	9.400	0.581	−0.0055	−0.0047	PI	No
75	+2σ	38.62	33.33	0.02	0.91	73.04	9.422	0.410	−0.0108	−0.0099	PI	No
75	+3σ	38.62	33.33	0.00	0.89	73.05	9.402	0.643	−0.0085	−0.0076	PI	No
80	−3σ	41.54	35.96	0.42	0.55	75.60	9.446	0.001	0.0195	0.0197	CC	No
80	−2σ	41.54	35.96	0.33	0.64	75.48	9.417	0.142	0.0155	0.0158	CC	No
80	−1σ	41.54	35.95	0.25	0.73	75.37	9.420	0.187	0.0056	0.0061	CC	No
80	0σ	41.54	35.98	0.16	0.81	75.25	9.400	0.495	−0.0022	−0.0015	PI	No
80	+1σ	41.54	35.97	0.08	0.88	75.15	9.400	0.617	−0.0091	−0.0083	PI	No
80	+2σ	41.59	36.13	0.02	0.90	75.07	9.418	0.458	−0.0135	−0.0127	PI	No
80	+3σ	41.59	36.14	0.00	0.88	75.05	9.422	0.373	−0.0140	−0.0132	PI	No
85	−3σ	44.51	38.80	0.41	0.56	80.13	9.415	0.117	0.0192	0.0195	CC	No
85	−2σ	44.51	38.81	0.33	0.65	80.00	9.417	0.148	0.0122	0.0126	CC	No
85	−1σ	44.51	38.81	0.24	0.73	79.88	9.421	0.201	0.0013	0.0019	CC	No
85	0σ	44.51	38.81	0.15	0.82	79.77	9.414	0.372	−0.0083	−0.0075	PI	No
85	+1σ	44.51	38.81	0.07	0.88	79.67	9.400	0.647	−0.0126	−0.0118	PI	No
85	+2σ	44.51	38.81	0.02	0.90	79.44	9.290	0.936	−0.0015	−0.0007	PI	No
85	+3σ	44.51	38.81	0.00	0.87	79.57	9.404	0.648	−0.0147	−0.0138	PI	No
90	−3σ	47.68	41.70	0.41	0.56	82.34	9.404	0.101	0.0151	0.0154	CC	No
90	−2σ	47.71	41.96	0.32	0.65	82.07	9.419	0.160	0.0070	0.0075	CC	No
90	−1σ	47.71	41.95	0.23	0.74	81.85	9.408	0.331	−0.0024	−0.0017	PI	No
90	0σ	47.65	41.96	0.14	0.82	81.84	9.404	0.518	−0.0108	−0.0100	PI	No
90	+1σ	47.71	41.96	0.07	0.88	81.42	9.383	0.750	−0.0147	−0.0137	PI	No
90	+2σ	47.71	41.71	0.02	0.90	81.31	9.367	0.895	−0.0142	−0.0133	PI	No
90	+3σ	47.71	41.96	0.00	0.87	81.17	9.356	0.902	−0.0135	−0.0126	PI	No
95	−3σ	50.59	44.71	0.40	0.56	87.14	9.418	0.130	0.0131	0.0134	CC	No
95	−2σ	50.59	44.71	0.31	0.65	86.92	9.421	0.167	0.0035	0.0040	CC	No
95	−1σ	50.59	44.72	0.23	0.74	86.70	9.405	0.397	−0.0054	−0.0047	PI	No
95	0σ	50.59	44.72	0.14	0.82	86.46	9.353	0.776	−0.0101	−0.0093	PI	No
95	+1σ	50.59	44.72	0.06	0.88	86.25	9.340	0.909	−0.0136	−0.0127	PI	No
95	+2σ	50.59	44.72	0.02	0.89	86.09	9.332	0.928	−0.0130	−0.0121	PI	No
95	+3σ	50.59	44.72	0.00	0.86	85.98	9.332	0.910	−0.0130	−0.0122	PI	No
100	−3σ	53.61	47.60	0.40	0.57	92.10	9.418	0.138	0.0100	0.0104	CC	No
100	−2σ	53.61	47.61	0.31	0.66	91.88	9.420	0.175	0.0017	0.0023	CC	No
100	−1σ	53.61	47.32	0.22	0.74	91.70	9.402	0.444	−0.0076	−0.0068	PI	No
100	0σ	53.64	47.61	0.13	0.82	91.43	9.329	0.854	−0.0114	−0.0106	PI	No
100	+1σ	53.64	47.61	0.06	0.88	91.22	9.314	0.916	−0.0126	−0.0117	PI	No
100	+2σ	53.64	47.61	0.02	0.89	91.05	9.316	0.927	−0.0132	−0.0123	PI	No
100	+3σ	53.64	47.61	0.00	0.86	90.97	9.316	0.908	−0.0132	−0.0123	PI	No
105	−3σ	56.53	50.04	0.39	0.57	97.10	9.420	0.137	0.0084	0.0088	CC	No
105	−2σ	56.53	50.04	0.30	0.66	96.89	9.421	0.180	−0.0006	−0.0000	PI	No
105	−1σ	56.53	50.04	0.22	0.74	96.67	9.397	0.521	−0.0106	−0.0098	PI	No
105	0σ	56.53	50.05	0.13	0.82	96.44	9.326	0.861	−0.0134	−0.0125	PI	No
105	+1σ	56.58	50.04	0.06	0.88	96.24	9.300	0.916	−0.0123	−0.0115	PI	No
105	+2σ	56.58	50.37	0.01	0.88	96.03	9.298	0.925	−0.0125	−0.0116	PI	No
105	+3σ	56.58	50.04	0.00	0.85	95.98	9.299	0.906	−0.0125	−0.0116	PI	No
110	−3σ	59.82	53.19	0.39	0.57	102.06	9.421	0.145	0.0052	0.0057	CC	No
110	−2σ	59.82	53.19	0.30	0.66	101.83	9.421	0.209	−0.0063	−0.0056	PI	No
110	−1σ	59.82	53.20	0.21	0.75	101.62	9.385	0.644	−0.0127	−0.0118	PI	No
110	0σ	59.82	53.21	0.12	0.82	101.39	9.290	0.875	−0.0123	−0.0114	PI	No
110	+1σ	59.82	53.21	0.06	0.88	101.19	9.287	0.916	−0.0124	−0.0115	PI	No
110	+2σ	59.82	53.21	0.01	0.88	101.05	9.287	0.922	−0.0127	−0.0118	PI	No
110	+3σ	59.88	53.20	0.00	0.85	100.95	9.289	0.902	−0.0131	−0.0121	PI	No
120	−3σ	41.73	37.85	0.40	0.57	112.00	9.414	0.110	0.0228	0.0228	CC	Yes
120	−2σ	42.37	37.86	0.31	0.66	111.69	9.404	0.224	0.0147	0.0146	CC	Yes
120	−1σ	61.08	53.34	0.21	0.75	115.25	9.251	0.817	−0.0062	−0.0054	PI	No
120	0σ	42.96	38.08	0.14	0.82	111.26	9.410	0.384	−0.0057	−0.0057	PI	Yes
120	+1σ	42.87	37.79	0.06	0.88	111.13	9.400	0.610	−0.0093	−0.0092	PI	Yes

Table A2 – *continued*

M_{ZAMS} [M_{\odot}]	Rate	M_{He} [M_{\odot}]	M_{CO} [M_{\odot}]	$X_{\text{C-He}}$ Mass frac.	$X_{\text{O-He}}$ Mass frac.	M_{Pre} [M_{\odot}]	$\text{Log } T_{\text{c}}$ [K]	$X_{\text{O-C-Pre}}$ Mass frac.	$\langle \Gamma_1 \rangle_{\text{Core-}}$	$\langle \Gamma_1 \rangle_{\text{TOT-}}$	Fate	Dredge-up
120	$+2\sigma$	60.69	53.18	0.01	0.88	115.18	9.280	0.921	−0.0126	−0.0116	PI	No
120	$+3\sigma$	60.81	53.36	0.00	0.85	115.13	9.280	0.900	−0.0126	−0.0117	PI	No
140	-3σ	48.93	45.50	0.39	0.58	131.07	9.422	0.015	0.0389	0.0386	CC	Yes
140	-2σ	49.62	45.37	0.30	0.67	130.87	9.418	0.161	0.0092	0.0092	CC	Yes
140	-1σ	72.08	63.56	0.19	0.76	135.01	9.249	0.821	−0.0119	−0.0110	PI	No
140	0σ	72.85	64.31	0.11	0.83	134.84	9.244	0.869	−0.0119	−0.0109	PI	No
140	$+1\sigma$	73.92	65.67	0.05	0.87	134.98	9.239	0.884	−0.0115	−0.0106	PI	No
140	$+2\sigma$	72.85	64.47	0.01	0.86	134.85	9.243	0.884	−0.0118	−0.0109	PI	No
140	$+3\sigma$	72.41	63.95	0.00	0.83	134.55	9.250	0.867	−0.0132	−0.0122	PI	No
160	-3σ	56.94	53.57	0.37	0.58	149.97	9.434	0.020	0.0310	0.0308	CC	Yes
160	-2σ	57.54	53.54	0.28	0.67	149.75	9.443	0.019	0.0250	0.0248	CC	Yes
160	-1σ	58.08	53.80	0.19	0.76	149.55	9.435	0.042	0.0238	0.0237	CC	Yes
160	0σ	84.80	75.20	0.10	0.83	153.31	9.216	0.821	−0.0112	−0.0103	PI	No
160	$+1\sigma$	84.74	75.20	0.04	0.86	153.22	9.220	0.858	−0.0124	−0.0115	PI	No
160	$+2\sigma$	83.70	74.31	0.01	0.85	152.53	9.219	0.853	−0.0116	−0.0108	PI	No
160	$+3\sigma$	85.36	76.07	0.00	0.82	153.41	9.216	0.823	−0.0117	−0.0107	PI	No

Note. Column 1: ZAMS mass. Columns from 2 to 9 same as in Table A1. Column 10: $\langle \Gamma_1 \rangle_{\text{Core-}}$. Column 11: $\langle \Gamma_1 \rangle_{\text{TOT-}}$. Column 12: final fate of the star, which can be either core collapse (CC) or pair-instability (PI). Column 13: indicates if stars undergo dredge-up during the evolution.

APPENDIX B: PURE-HE PARSEC–MESA TRACKS COMPARISON

Fig. B1 shows the comparison between $40 M_{\odot}$ pure-He models with varying $^{12}\text{C}(\alpha, \gamma)^{16}\text{O}$ rates computed in this work and pure-He models of $40 M_{\odot}$ computed by Farmer et al. (2020) with MESA stellar evolutionary code. The MESA tracks evolve until the final core collapse, but in the figures we show only tracks until $\text{Log}(T_{\text{c}}/\text{K}) = 9.5$ or $\langle \Gamma_1 \rangle = 4/3$. In spite of a different assumed treatment by the two codes for convection, winds, opacity, and other physical processes, the evolution during the CHeB phase of the two sets of models is very similar (as shown in $\langle \Gamma_1 \rangle - T_{\text{c}}$ and $\rho_{\text{c}} - T_{\text{c}}$ diagrams). PARSEC and MESA models computed with $+3\sigma$ show a very similar evolution during all the burning phases and they both become unstable shortly after oxygen ignition. When $\langle \Gamma_1 \rangle$ reaches $4/3$, PARSEC and MESA models have a M_{Pre} of 38.7 and $39.8 M_{\odot}$, respectively. The MESA model follows the evolution through the PPI, in which the star loses mass and then returns dynamically stable. After the pulsating phase, the star undergoes the final core collapse leaving a BH of $34.8 M_{\odot}$.

PARSEC and MESA models with 0σ and -3σ start to behave differently after the ignition of carbon in the core. During the core carbon burning phase, the MESA model with 0σ develops an interaction between the external part of the carbon core and the bottom of the He envelope, that extracts C from the core. This core–envelope interaction stabilizes the model that avoids the PPI and evolves directly to the CC, leaving a BH of $39.8 M_{\odot}$ (Table B1). The correspondent PARSEC model does not undergo the core–envelope interaction and the model becomes unstable after the ignition of oxygen in the core. This model enters the PPI regime. After the depletion of carbon in the core, both PARSEC and MESA models with -3σ start to burn carbon in a shell above the stellar centre. As already discussed in Section 4.1, the C burning shell sustains the stellar envelope and prevents the collapse of the star, allowing the core oxygen burning in a non-explosive way. At the end of the oxygen burning, the PARSEC model has $M_{\text{Pre}} = 38.9 M_{\odot}$ and can evolve until the final CC. The MESA model follows the evolution through the core collapse and the final black hole mass is $M_{\text{BH}} = 39.8 M_{\odot}$. Table B1 lists some properties of the $40 M_{\odot}$ pure-He MESA models.

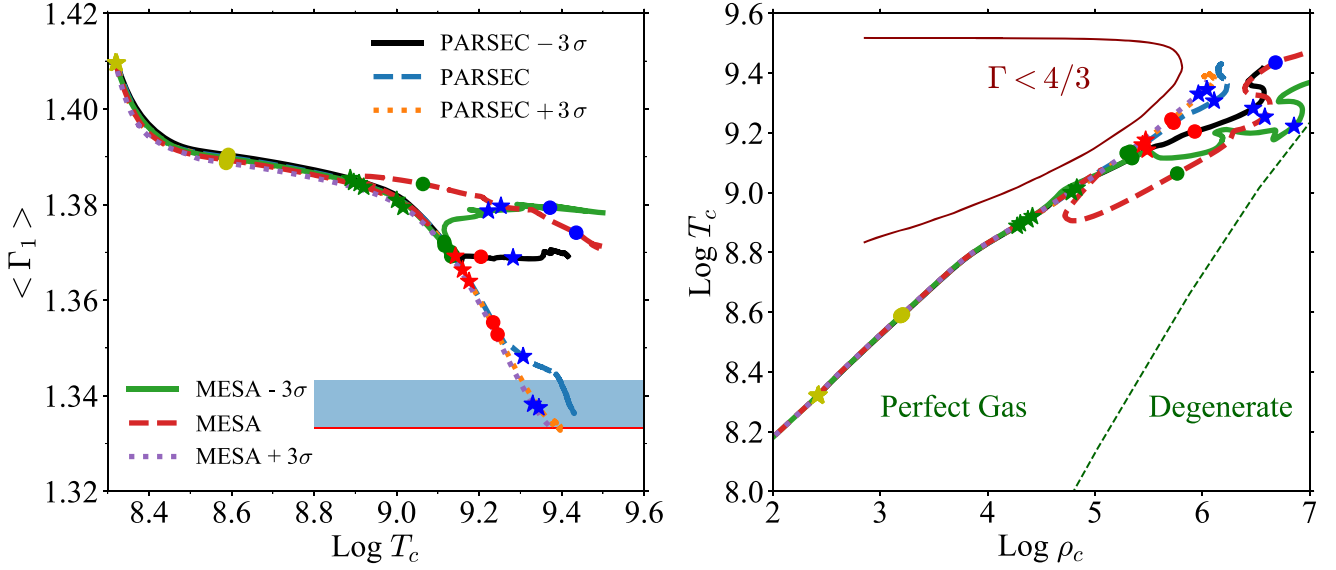


Figure B1. Left-hand panel: Evolution of the weighted first adiabatic exponent, $\langle \Gamma_1 \rangle$, of $M_{\text{He-ZAMS}} = 40 M_{\odot}$ pure-He stars computed with MESA and PARSEC evolutionary codes. MESA tracks are from sets computed by Farmer et al. (2020). Solid lines indicate tracks computed with -3σ rates, dashed lines show tracks with 0σ , while dotted lines indicate tracks with $+3\sigma$. The red line indicates $\langle \Gamma_1 \rangle = 4/3$. The blue region indicates the zone between $4/3$ and $4/3 + 0.01$, zone in which we consider our tracks unstable. Right-hand panel: ρ_c - T_c diagram of same tracks of the left-hand panel. In both the left-hand and right-hand panels we use the same symbols as in Figs 5 and 10.

Table B1. Pure-He models' with $40 M_{\odot}$ from (Farmer et al. 2020). See text for details.

Rate	M_{He} [M_{\odot}]	M_{CO} [M_{\odot}]	$X_{C_c - \text{He}}$	$X_{O_c - \text{He}}$	M_{BH} [M_{\odot}]	Fate
-3σ	39.87	35.39	0.37	0.59	39.86	CC
0σ	39.86	35.26	0.12	0.84	39.85	CC
$+3\sigma$	39.84	35.07	<0.01	0.86	34.85	PI

Note. The first column reports the rate assumed for the $^{12}\text{C}(\alpha, \gamma)^{16}\text{O}$ reaction, the second and third ones report the masses of the helium core and CO core at the end of the He-MS, respectively. The fourth and fifth columns list the carbon and oxygen central mass fractions at the end of the He-MS. The sixth column shows the final black hole mass (M_{BH}), and the last column reports the final fate of the star: core collapse (CC) or pair instability (PI).

This paper has been typeset from a \LaTeX file prepared by the author.